Shamsian et al. *Microsystems & Nanoengineering* (2025)11:127
https://doi.org/10.1038/s41378-025-00898-3

Microsystems & Nanoengineering
www.nature.com/micronano

REVIEW ARTICLE Open Access

Nanomaterials in PCR: exploring light-to-heat conversion mechanisms and microfluidic integration

Samaneh Shamsian[1], Abu Bakar Siddique[1], Vahid Kordzadeh-Kermani[1], Luna de la Vega Tejuca[1], Francisco Falcone[1,2], Mallar Ray[1], Seyed Nezameddin Ashrafizadeh[3], Sergio Omar Martínez Chapa[1], Marc J. Madou[1,4] and Masoud Madadelahi[1]✉

Abstract

As a popular process in molecular-based diagnostics, polymerase chain reaction (PCR) can be employed for amplifying small amounts of DNA/RNA from different sources such as tissue, cells, peripheral blood and so on. Thanks to the unique physicochemical characteristics of nanomaterials and their progress, researchers have been encouraged to employ them as suitable candidates to address the PCR optimization challenges for enhancing efficiency, yield, specificity, and sensitivity. In nanoparticle-assisted PCR (nanoPCR), different nanoparticles (NPs) such as carbon nanotubes (CNTs), graphene, quantum dots (QDs), and gold (Au) might be used. Among different nanoPCR assays, photothermal PCR has emerged as a technique leveraging the excellent light absorption and heat conversion capabilities of nanomaterials. In addition to presenting recent advances in nanoPCR, this review also delves into the specific use of nanomaterials for photothermal PCR, including their applications in microfluidics as one of the best platforms for miniaturization of diagnostic techniques. Different types of NPs used in PCR are comprehensively examined, and detailed charts and tables are provided that outline features such as optimal concentration and size. The appropriate choice of nanomaterials for enhancing light conversion to heat in PCR applications is discussed. Finally, the related challenges and future trends are explored.

Introduction

The polymerase chain reaction (PCR) is utilized as a prevalent strategy to rapidly amplify target nucleic acid structures outside of living organisms. Numerous industries have revealed an extensive range of applications for this technique, such as food safety[1], clinical testing[2], archaeological examinations[3], and biological studies[4]. There are different inhibitors and facilitators to manipulate PCR performance[5]. The principal inhibitor in PCR is interference between chemicals and DNA polymerase, nucleic acids (template DNA/primer sequences), or nucleotides (dNTPs)[6]. The components of human blood such as heme, hemoglobin, lactoferrin, and immunoglobin G[7–9]; hair and skin melanin and eumelanin[10,11]; organic molecules in soil such as humic and tannic acids[12,13]; monomeric proteins found in muscle tissue such as myoglobin[14]; collagen and calcium ions in milk[15,16]; substances originated from foods such as complex polysaccharides which are presented in feces[17,18]; and urea found in urine[19] are instances of widely used PCR inhibitors. In contrast, the main classifications of PCR facilitators are non-ionic detergents, proteins, organic solvents, extra polymerase enzymes in the presence of enzyme-targeting inhibitors, biological matrices and polymers, PCR cocktails containing more than one additive (e.g., 1,2-propanediol-trehalose (PT) combination),

Correspondence: Masoud Madadelahi (masoud.m@tec.mx)
[1]School of Engineering and Sciences, Tecnologico de Monterrey, Monterrey 64849 NL, Mexico
[2]Department of Electrical, Electronic and Communication Engineering and the Institute of Smart Cities, Public University of Navarre (UPNA), 31006 Pamplona, Spain
Full list of author information is available at the end of the article
These authors contributed equally: Samaneh Shamsian, Abu Bakar Siddique

and nanoparticles (NPs) (e.g., carbon nanotubes (CNTs), metal/metal oxides, and quantum dots (QDs)[6]). NPs are very efficient in facilitating PCR owing to their exceptional characteristics, including their small size, excellent thermal conductivity, high surface-to-volume ratios, and dense surface electric charge[20,21]. The nanoPCR technique involves the integration of NPs with PCR reagents, which primarily consist of enzymes, templates, and primers. The kinds of nanomaterials utilized in PCR up to now consist of metals (like gold (Au)[22] and silver (Ag)[23]), carbons (like CNTs[24], carbon nanopowders (CNPs)[25], diamond[26], and graphene NPs[27]), oxides (like zinc oxide (ZnO)[28], titanium dioxide (TiO_2)[29], and graphene oxide (GO)[30]), and other materials like QDs[31].

Photothermal conversion—the action of absorbing photon energy and converting it into thermal energy—is one of the applications of NPs in PCR[32]. The photoexcited material's capacity to capture light and its efficiency in converting to heat are two crucial criteria that account for the photothermal conversion efficiency[33]. As viable candidates for photothermal catalysis, a wide variety of substances have been investigated to date, including metallic nanostructures[34,35], semiconductors[36,37], carbon-based nanomaterials[38–41], organic polymers[42,43], and more recent materials like metal-organic frameworks (MOFs)[44–48], 2D carbides or nitrates of transition metals (MXenes)[49–51], and covalent organic frameworks (COFs)[52–55]. Considering the diversity in the physicochemical characteristics of nanomaterials, photothermal conversion is improved through three mechanisms: plasmonic localized heating, nonradiative relaxation of excited carriers, and molecular vibrations. Metals exhibit plasmonic localized heating, which increases the radiative scattering and absorption of resonant light when the collective oscillation of the free electrons is driven coherently by the oscillating electric field of light. Semiconductors primarily observe the nonradiative relaxation of excited carriers, which absorbs photon energy surpassing their bandgaps. This process converts energy into heat by facilitating the excitation of electrons from the valence band to the conductive band. Next, in the valence band and conduction band, respectively, excitation-state electrons and holes are generated. The electrons and holes in the excitation state then relax to the matching edges of the conductive band and valence band. Thus, the energy is effectively transformed into heat[56]. The photothermal mechanism through vibrational modes is another technique that occurs in polymer-based and carbon-based nanomaterials[57–60]. This mechanism involves light absorption, which excites electrons of the highest occupied molecular orbital (HOMO) to jump to the lowest unoccupied molecular orbital (LUMO)[61], leading some of the excess energy of these excited electrons to be subsequently transferred to the surrounding lattice molecules. This transferred energy induces molecular vibrations, which generate heat. It is important to note that photothermal performance can be significantly improved with well-designed nanomaterials. Nanomaterials can be employed with either a single- or multi-component structure providing photothermal mechanisms.

NanoPCR assays integrated with microfluidics play an essential role in improving the specificity, amplification efficiency, sensitivity, and detection accuracy of diagnostic tests. These techniques, with main advantages such as shortened reaction duration, low reagent utilization, and the capability to manage multiple assays simultaneously on a single disk, are superior to conventional methods. The ability of low-abundance biomarker detection is another benefit of the incorporation of NPs into microfluidics, which enables rapid and early disease detection[62–64]. In this review, we extensively discuss the state-of-the-art nanoPCR processes alongside the implementation of light-to-heat converter NPs in microfluidic devices. Figure 1 shows the frequency of published publications regarding PCR: the red columns represent the number of PCR papers with NPs, the orange columns represent the microfluidic PCR papers' numbers, and the black columns represent the number of PCR papers with a photothermal effect. The rapid rise of publications on each of the three topics underlines the necessity of this review. In the following sections, we examine nanoPCR assays, and their roles in improving specificity, sensitivity, yield, and efficiency are discussed. The principles of light-to-heat conversion through localized surface plasmon resonance (LSPR), nonradiative relaxation, and molecular vibrations are presented. In order to understand the basic concepts for the design of photothermal NPs, mathematical principles underlying light-to-heat conversion are presented. We evaluate the photothermal efficiency of different nanostructured materials in biological contexts and highlight recent advancements in photothermal conversion for PCR applications, including the latest developments in on-chip PCR using photothermal nanomaterials.

NanoPCR

Denaturation, annealing, and extension are the three primary stages in each thermal cycle of a PCR reaction (Fig. 2). During the denaturation phase, increasing the temperature up to a high range of 94–98 °C allows the DNA strands to split. During the annealing step, when the temperature is decreased to 50–65 °C, short primers can be attached to the target DNA sequence. Finally, primers offer DNA polymerase a starting point to connect dNTPs and create new complementary DNA strands during the extension process around the temperature of 72 °C. By repeating this process for a certain number of PCR cycles (n times) with a controlled heat cycling speed, the number

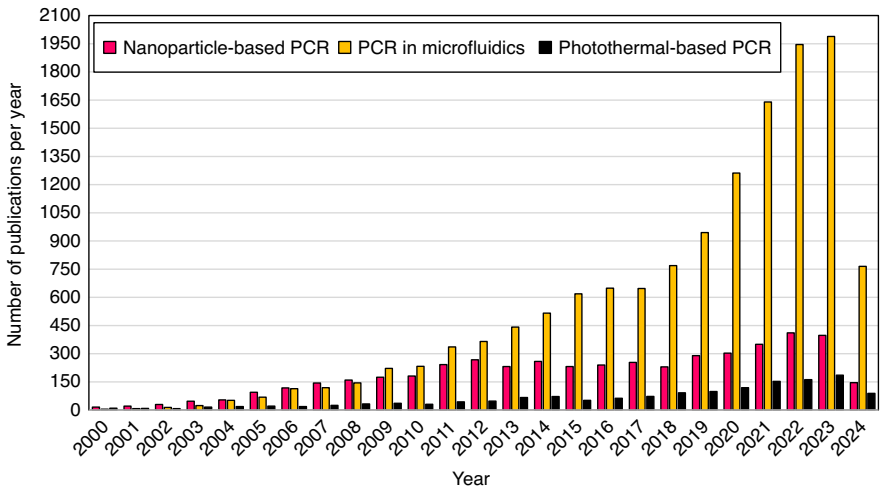

Fig. 1 The annual number of papers published on various topics, including "nanoparticle-based PCR," "PCR in microfluidics," and "photothermal PCR," as determined using Scopus database keywords. The keywords "nanoparticle PCR" and "nanoPCR" are represented in red, "microfluidics-based PCR" and "on-chip PCR" in orange, and "photo PCR," "photothermal PCR," "light-to-heat PCR," and "plasmonic PCR" in black

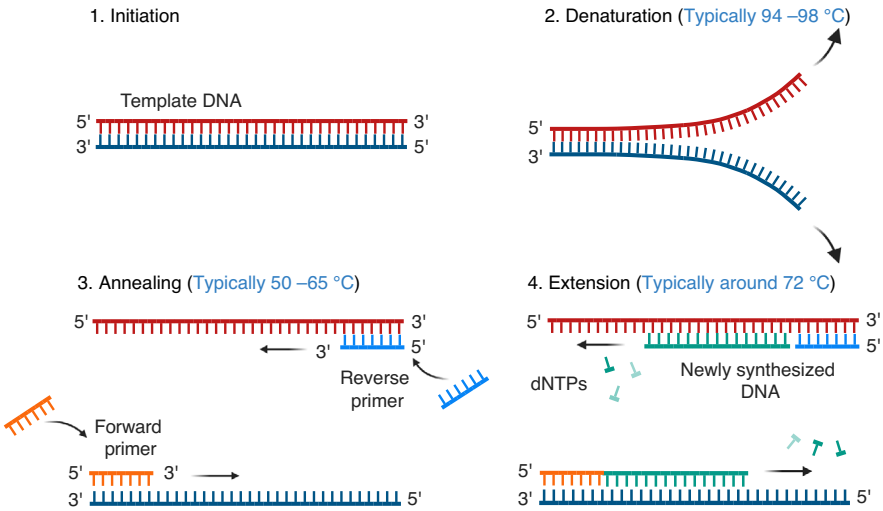

Fig. 2 Main stages in the PCR process: (1) preparation of double-stranded DNA; (2) denaturation of double-stranded DNA into single-stranded DNA; (3) annealing of short primers to the start and end of the target DNA sequence; and (4) extension of the newly synthesized DNA by attaching dNTPs to the ends of the primers

of DNA strands can be amplified efficiently and precisely. In theory, the exponential function of 2^n is commonly expressed to count the number of DNA rises during the PCR process[5,65].

The detection limit and amplification efficiency of PCR can be affected by the intervention of chemicals in polymerase enzymes or their impact on primers, DNA templates, and dNTPs[66]. The presence of PCR facilitators during sample preparation can potentially manipulate the PCR performance[5]. NPs act as one of the best PCR facilitators due to several important mechanisms: they possess excellent thermal conductivity, demonstrate catalytic features, are similar to single-stranded DNA-binding proteins (SSBs), and participate in electrostatic/surface interactions with PCR components[67,68]. NP-assisted PCR assays with excellent thermal conductivity exhibit improved reaction duration and efficient heat transfer[69]. The catalytic activity of NPs facilitates the PCR process even under conditions below the optimal environmental standards[67]. Modifying the negatively charged surface of NPs with carboxyl groups improves the amplification specificity in the PCR process. It minimizes

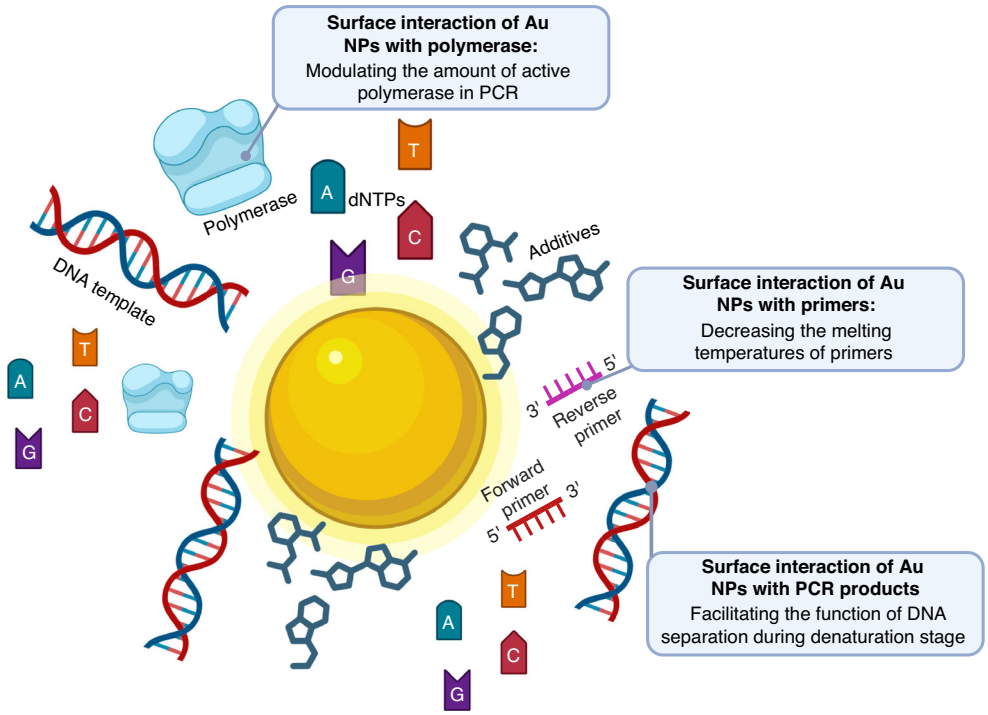

Fig. 3 Three ways in which Au NPs impact the PCR include: (1) decreasing the PCR's active polymerase concentration; (2) effectively inhibiting the primer mismatch and formation of nonspecific amplification by decreasing the melting temperatures of the primers; and (3) efficiency improvement and enabling the PCR to run effectively in a faster heat cycler by accelerating the PCR products' dissociation rate

the risk of mispairing between templates and primers by selectively binding to single-stranded DNA in a similar optimization technique to SSBs[31]. Electrostatic interactions between the positive and negative charges of NPs and PCR components, respectively, play a crucial role in increasing the stability of PCR components and enhancing the efficiency and specificity of PCR[70–72]. In terms of surface interactions, NPs have an impact on PCR in three ways: interaction with polymerase, influencing primers, and template DNA[73]. Using Au NPs as an illustration (Fig. 3), the adsorption of polymerase by Au NPs regulates the amount of active polymerase in PCR. Au NPs improve PCR specificity by adsorbing primers and increasing the difference in melting temperatures between complementary and mismatched primers. PCR products are adsorbent, and Au NPs assist them to be separated during the denaturing stage[68]. Understanding the characteristics and properties of the surface of NPs facilitates their selection and optimization for PCR amplification. So far, many NPs have been reported to enhance PCR efficiency and speed up the PCR process, like Au[22,74,75], CNT[76], Ag[77], QD[78], GO[79], metal oxides (e.g., TiO_2, ZnO, and magnesium oxide (MgO))[80], and composites. By applying the proper concentration of NPs, they can improve PCR specificity and provide products with enhanced bands. Since low concentrations of NPs inhibit the amplification of long fragments, while high concentrations inhibit the amplification of small fragments and disturb the PCR reaction, it is important to carry out the nanoPCR process with the optimal concentration of NPs[73,81]. Table 1 lists the effects of NPs of optimal size and concentration that improve the PCR process, and Table 2 illustrates nanoPCR applications in different fields.

In Fig. 4, we show the size ranges of different NPs from the literature for PCR applications. Au NPs can be as large as 100 nm, which is over five times the size of other metal NPs utilized in PCR. In terms of size ranges, carbon nanostructures are comparable to metals, with the highest size ranging from 30 nm to 70 nm for CNT/PEI composites and the smallest size of 1 nm for CNTs. To date, the reported optimal sizes for ZnO (35–1000 nm) in the oxide group, PDA (177–328 nm), and ADACP (250–350 nm) in the other composites have been considerably broader than the size ranges for metals and carbons. PEG-nGO and SCM are two other NPs that exhibit optimal sizes of 200 nm and 1000 nm, respectively, which are larger compared to other NPs in the metal and carbon groups.

In Fig. 5, the optimal concentrations of various NPs for PCR applications are shown. It is clear that Au, TiO_2, CNT-X (such as MWCNT-Fe_3O_4, CNT/PEI, and NH_2-SWCNTs), and graphene-X (such as GO, GNFs, and GO-Au) with the optimum concentration ranges of 0.19 ×

Table 1 List of nanomaterials applied as PCR enhancers

Group	Type of NPs	Size (nm)	Optimum concentration	Advantages/disadvantages	Template length (bp)	Refs.
Au NPs	Au	13	0.7 nM	–Increase the PCR yield by 10^4–10^6-fold and decrease the time of reaction.	–	69
	Au	10	0.4 nM	–Improve the specificity upon the addition of 0.4–0.8 nM Au NP.	283	205
	Au	10	0.19 nM; 0.23 nM	–Increase the PCR yield, specificity, and efficiency.	–	206
	Au	10	Dependent on polymerase concentration.	–Specificity and efficiency (favor smaller products).	309	207
	Au	25	16.3 mg/L	–Increase the PCR efficiency and specificity.	124	208
	Au	~11	2 nM	–Increase the PCR yield.	–	209
	Au DENPs[a]	1.9–2.6	0.37 nM	–Increase the PCR efficiency and specificity.	283	210
	PDDA[b]-Au	12	1.54 pM	–Increase the PCR efficiency and specificity.	283	70
	PEG–Au PE[c]	4.5–6.9	Dependent on the molar ratio between Au atom and PEI.	–Increase the PCR efficiency and specificity.	283	71
Carbon	SWCNTs[d]	2	3 g/L	–Increase the PCR yield.	410	24
	SWCNTs	1–2	1 g/L	–Increase the long PCR efficiency and specificity.	14.3 kb	211
	MWCNTs[e]	<8	1 g/L	–Increase the long PCR efficiency and specificity.	14.3 kb	211
	CNT/PEI[f]	D: 30–70; L: 0.1–2 µm	CNT/PEI.Ac: 0.39 mg/L; CNT/PEI.SAH: 630 mg/L	–Increase the PCR efficiency and specificity.	283	212
	NH_2-MWCNTs	D: 13–18; L: 1–12 µm	CNT/PEI.Ac: 630 mg/L; CNT/PEI.SAH: 23 mg/L	–Increase the PCR specificity and efficiency up to 70% (filtered NH_2-MWCNT).	96	213
	NH_2-SWCNTs	D: 1–5 nm; L: 1–5 µm	31 mg/L	–Increase the PCR yield.	283	214
	CNP	30 nm	1 g/L	–Increase the PCR specificity and efficiency in a repeating process of PCR and long-time PCR approaches.	540	25
	GNFs	Thickness: 8 nm	1 g/L	–a 65% decrease in cycle numbers and an increase in the PCR efficiency.	1248	215

Table 1 continued

Group	Type of NPs	Size (nm)	Optimum concentration	Advantages/disadvantages	Template length (bp)	Refs.
	Graphene	–	12 mg/L	–Increase the PCR specificity.	300	27
Oxide NPs	TiO_2	20	–	–Increase the DNA synthesis inhibition.	650	29
	TiO_2	~25	0.4 nM	–50% decrease in overall PCR time; 7-fold increase in the produced amount of PCR product; and improve the efficiency of PCR.	–	216
	TiO_2	7	0.2 nM	–Increase the PCR efficiency by three or more-fold.	–	80
	TiO_2	100	0.2 g/l	–a 50% reduction in the overall PCR time and an increase in DNA purity.	–	217
	TiO_2	4.821	1.6 g/L	–Eliminate the non-specific bands or false negatives occurrence.	–	218
	Fe_3O_4	8–10	1.3 g/L	–Low limit of detection (LOD) of 4.26 aM; ultrafast DNA detection, and decrease the non-specific products.	41	219
	Fe_3O_4	33	0.72×10^{-2} nM	–190% increase in the PCR yield.	800	220
	Silica-coated and ZnO (amino-modified)	D:80 nm; L: 5–10 µm	10 mg/L	–Increase the PCR yield.	–	28
	ZnO	35	0.4 g/L	–A 50% decrease in total reaction time and an increase in DNA purity and efficiency.	–	217
	GO	Thickness: 1 nm	1 mg/L	–Increase the PCR specificity.	283	30
	SiO_2	271	–	–Improve the quantity of PCR products.	100	221
Others	CdTe QDs	2–10	4 nM	–Increase the PCR specificity even for a long sequence template and no enhancement on the PCR efficiency.	297, 594, 1003, 8000	31
	CdTe QDs	3–4	80 nM	–Reduce the PCR time and achieve excellent effects on hot-start PCR.	~1000	222
	CdTe QDs	–	67 nM	–Retained PCR specificity in the ninth round of amplification.	143, 284, 111, 215, 279, 400	223
	Graphene QDs (GQDs)	40	0.06 mg/L; 0.08 mg/L	–Increase the PCR yield, specificity, and efficiency.	100	224
	PDA[g]	177–328	0.1 g/L	–Increase the PCR efficiency and high sensitivity with the detection limit of 6.7×10^4 CFU/mL.	–	225
	C–PDA silica	271	2.5 pg/µL	–High-performance PCR in both the short and long DNAs.	248, 800	221
	PEG-nGO[h]	200	5 mg/L	–Increase the PCR efficiency and specificity.	110	226

Table 1 continued

Group	Type of NPs	Size (nm)	Optimum concentration	Advantages/disadvantages	Template length (bp)	Refs.
	GO-Au hybrid composite	15.2	–	–Broad range of annealing temperatures and increase the PCR efficiency.	200, 800	72
	MOFs	–	20 mg/L	–Wide range of annealing temperatures and increase the PCR efficiency and specificity.	48,502	227

[a]Dendrimer-entrapped Au NP
[b]Poly (diallyl dimethylammonium) chloride
[c]Polyethylene glycol (PEG) modified polyethyleneimine (PEI) entrapped Au NPs
[d]Single-walled CNTs
[e]Multi-walled CNTs
[f]PEI-modified MWCNTs
[g]Polydopamine NPs
[h]Polyethylene glycol engrafted nanosized graphene oxide

10^{-6}–0.4 mM, 0.2 × 10^{-6}–2 mM, 390 × 10^{-6}-0.63 g/L, and 40 × 10^{-6}–1 g/L, respectively, are the most commonly used nanomaterials in PCR. The optimal concentrations of other NPs like ZnO nanoflowers (1 mM), CNPs (1 g/L), SWCNTs (1–3 g/L), and MWCNTs (1 g/L) have been observed at high values. CuO, ZnO, Al_2O_3, Fe_3O_4, and PDA have been seldom employed for PCR, and the reported optimal concentrations for them are also low.

Light-to-heat conversion mechanisms using NPs

With NPs, one can convert the energy of incoming light into heat energy by releasing the absorbed photon energy into the surrounding environment[32]. In photothermal conversion, there are three main processes that are very important: the plasmonic effect in metals, the non-radiative energy scattering of excited electron–hole pairs in semiconductors, and molecular vibrations. This section offers a comprehensive analysis of the three principal photothermal processes, as they represent the core principles of photothermal conversion, focusing on the various types of NPs. These NPs are crucial for photothermal conversion, with each category - metallic, semiconducting, and carbon-based exhibiting one or more of these photothermal mechanisms.

Plasmonic localized heating is an optical phenomenon that is mainly associated with the metal NPs, which occurs when the plasmonic resonance on the surface of metallic NPs is subjected to an electromagnetic wave with a wavelength much larger than their size. The incident electric field strongly interacts with the conduction electrons of the metal NPs, leading to their collective oscillation (Fig. 6a (left))[82]. The absorption of incoming light is further intensified at the resonance frequency, resulting in highly amplified electric fields near the surface of the NPs. This phenomenon is known as LSPR[83].

The ability for metal NPs to modify LSPRs across a wide range of the electromagnetic spectrum, from the visible to the infrared, attracted a lot of attention for plasmonic localized heating[84,85]. The steps involved in achieving localized heating via LSPR are summarized in the schematic of localized plasmonic heating in Fig. 6a (right). (1) Excitation: The stimulation of plasmons has the potential to amplify the electric field intensity at the NP surface, resulting in significant absorption and scattering cross-sections at resonance frequencies. (2) Rapid heating: The nonequilibrium rapid heating of metal NPs occurs when they are activated by resonant photons, leading to the photoexcitation of the electron gas. (3) Relaxation: The electric excitation is followed by relaxation at timescales less than a picosecond, which occurs through electron-electron scattering facilitated by the Landau damping effect. (4) Rapid temperature rise: Electron-electron scattering leads to a fast elevation in the metal's surface temperature. (5) Heat dissipation in the surrounding

Table 2 NanoPCR applications

Group	Type of NP	Size (nm)	Optimum concentration	Advantages/disadvantages	Type of detection	LOD	Temp length (bp)	Refs.
Virus Detection	Solid NPs	1–100	–	–A 100-fold increase in the PCR sensitivity and an increase in the PCR efficiency.	Porcine parvovirus (PPV)	56 copies/μL	1989, 142	[228]
	Solid Au NPs	1–100	–	–100–1000-fold increase in PCR sensitivity; 10.4% increase in detection rate; and rapid and sensitive diagnostic tool.	Detection and differentiation of pseudorabies vaccine strains (gene-deleted and wild-type)	gB, gE, gG: 10, 10, 10^2 10, 10, 10^4 copies	-	[229]
	Au NPs Solid form (colloidal nanofluids)	1–100	–	–100-fold increase in the PCR sensitivity; 16.8% and 59.7% increase in detection rate.	Porcine bocavirus	67 copies/μL	482	[230]
	Au NPs Solid form (colloidal nanofluids)	1–100	–	–100-fold increase in the PCR sensitivity.	Porcine epidemic diarrhea virus (PEDV)	2.7×10^{-6} ng/μL	-	[231]
	NP	–	–	–100-fold increase in the PCR sensitivity and 56.3% increase in detection rate.	Mink enteritis virus (MEV)	87.5 copies/μL	-	[232]
	Solid Au NPs form colloidal nanofluids	1–100	–	–100–1000-fold increase in the PCR sensitivity; rapid and specific nanoPCR; and 98.1% consistency in detection rate.	Virus infections (Concurrent of pseudorabies and porcine bocavirus)	PRV: 6; PRV: 9 copies/μL	996, 316	[233]
	Au	15	1 nM	–A 100-1000-fold increase in the PCR sensitivity and a high-yield amplification.	Herpes virus-1 (EHV-1)	10^2 copies/μL	188	[234]
	Solid Au NPs form colloidal nanofluids	1–100	–	–A 100-fold increase in the PCR sensitivity and an increase in the PCR specificity.	Encephalomyocarditis virus	1.2×10^2 copies/μL	-	[235]
	Solid NPs	1–100	–	–A 10-fold increase in the PCR sensitivity and an increase in the PCR specificity.	Porcine epidemic diarrhea and transmissible gastroenteritis viruses	PEDV: 76; TGEV: 85; copies/μL	182, 278	[236]
	Au	20, 23, 40	–	–10-fold increase in the PCR sensitivity.	Bovine respiratory syncytial virus	1.43×10^2 copies/μL	19, 21	[237]
	Au NPs	10	–	–A 100-fold increase in the PCR sensitivity and an increase in the PCR specificity.	Rotavirus, Parvovirus Bovine, and Viral Diarrhea of Bovine Viruses	9.4×10^2; 5.14×10^3; 4.09×10^1 copies/μL	235, 1172, 2022	[238]
	NPs of Solid Au	1–100	–	–A 10-fold increase in the PCR sensitivity and an increase in the PCR specificity.	DNA of HPV-18 and HPV-16	1.7 copies/μL	-	[239]

Table 2 continued

Group	Type of NP	Size (nm)	Optimum concentration	Advantages/disadvantages	Type of detection	LOD	Temp length (bp)	Refs.
	Au NPs (colloidal nanofluids)	1–100	–	–100-fold increase in the PCR sensitivity and no improvement in detection rate.	Canine coronaviruses I and II distinguishing	CCoV II, I: 6.91×10^2, 6.47 copies/μL	-	[240]
	Au (Solid NPs)	1–100	–	–100-fold increase in the PCR sensitivity; 50% increase in detection rate; and high specificity.	canine coronavirus, distemper,and parvovirus (CCV, CDV, CPV)	CDV, CPV, CCV: 5.4×10^2 6.5×10^2 1.6×10^2 copies	-	[241]
	Au NPs	30	0.4 mM	–9.7% increase in detection rate and specificity of 73%.	Goose Parvovirus (GPV)	4.68×10^2 copies/μL	389	[242]
	Au NPs	30	0.3 mM	–A 25.5% increase in detection rate and an increase in the PCR specificity.	Feline Panleukopenia Virus (FPV)	7.97×10^2 copies/μL	345	[243]
	CNTs	1	10 mg/L	–80% increase in nanoPCR-based detection sensitivity.	SARS-CoV-2 coronavirus	6.4 copies/μL	-	[244]
	MgO	50	275 mg/L	–13-fold increase in the PCR sensitivity; 26.5% decrease in PCR time; and decrease the cycle number to 25 cycles.	Tomato leaf curl virus	0.01 ng	100	[245]
	Ag-MgO	Ag: 20; MgO: 50	Ag: 3; MgO: 275 mg/L	–12-fold increase in the PCR sensitivity.	Tomato leaf curl virus	0.01 ng	100	[245]
	GO–Au	15	10 mg/L	–~1000-fold increase in detection limit of real-time PCR; remarkable sensitivity and selective detection.	The disease of Foot-and-Mouth Virus (FMDV)	1 pg	-	[246]
	MWCNT-Fe_3O_4	15	5 mg/L	–Increase the PCR sensitivity.	Epstein–Barr virus (EBV)	$1:10^7$ fold	-	[247]
	ZnO Nanoflowers	1000	1 mM	–Decrease the PCR time and increase the PCR specificity and sensitivity.	Quick Diagnosis of Canine Vector-Borne Pathogens	–	619, 666	[248]
	SCM- ADACP[a]	SCM:1000; ADACP: 250-350	SCM: 10; ADACP: 5 g/L	–Visual detection by the naked eye and high sensitivity and specificity.	Hepatitis C virus (HCV)	10 IU/mL	157	[249]
	Au NPs	60	–	–10-100-fold increase in detection limit; 60%, 71.4%, and 76.9% increase in detection rate of FCP, FPV, and FHV-1, respectively.	Viruses: Feline calicivirus, herpesvirus type-I, and panleukopenia syndrome	FCP, FPV, FHV-1: 2.97×10^1 2.64×10^4 2.85×10^1 copies/μL	-	[74]
	Ag	10–16	0.068 nM	–Decrease non-specific amplification and increase the PCR yield.	Strain Typing of Salmonella typhi	–	495	[23]

Table 2 continued

Group	Type of NP	Size (nm)	Optimum concentration	Advantages/disadvantages	Type of detection	LOD	Temp length (bp)	Refs.
Bacteria Detection	Au NPs	25	0.248 nM	–Decrease non-specific amplification and increase the PCR yield.	Strain Typing of Salmonella typhi	495	–	23
	Ag; TiO_2; Ag-TiO_2	–	Ag: 0.9; TiO_2: 0.6 nM	–Improve the efficiency of the PCR and its specificity; 500-fold increase in materials detection with low quantity; and decrease the amplification time.	Bacterial aerosols	40 pg/µL	–	250
	GO; CuO; Al_2O_3	GO: 20; CuO: 20; Al_2O_3: 20	GO, CuO, Al_2O_3: 0.4, 0.04, 0.4 0.4, 0.4, 0.4 0.04, 4, 0.04 mg/L	–Increase the PCR efficiency.	Brain-eating amoebae	0.004 µg/mL	–	251
Tumor Monitoring	Au NPs	14.33	50 nM	–Covering a wide range of concentrations (10^{-9}–10 µM) and mutation detection abundance in low values (e.g., 0.95% in spiked samples).	Monitoring of tumor mutations in a single-base)	0.95%	445	252
	GO	3	9.71 mg/L	–Increase the qRT-PCR sensitivity and specificity.	Monitoring of ovarian cancer by detection of miRNAs	10^1–10^9 copies/µL	94	79

[a]Magnetic particles (Streptavidin-coated) and polystyrene particles (anti-digoxigenin/body-coated)

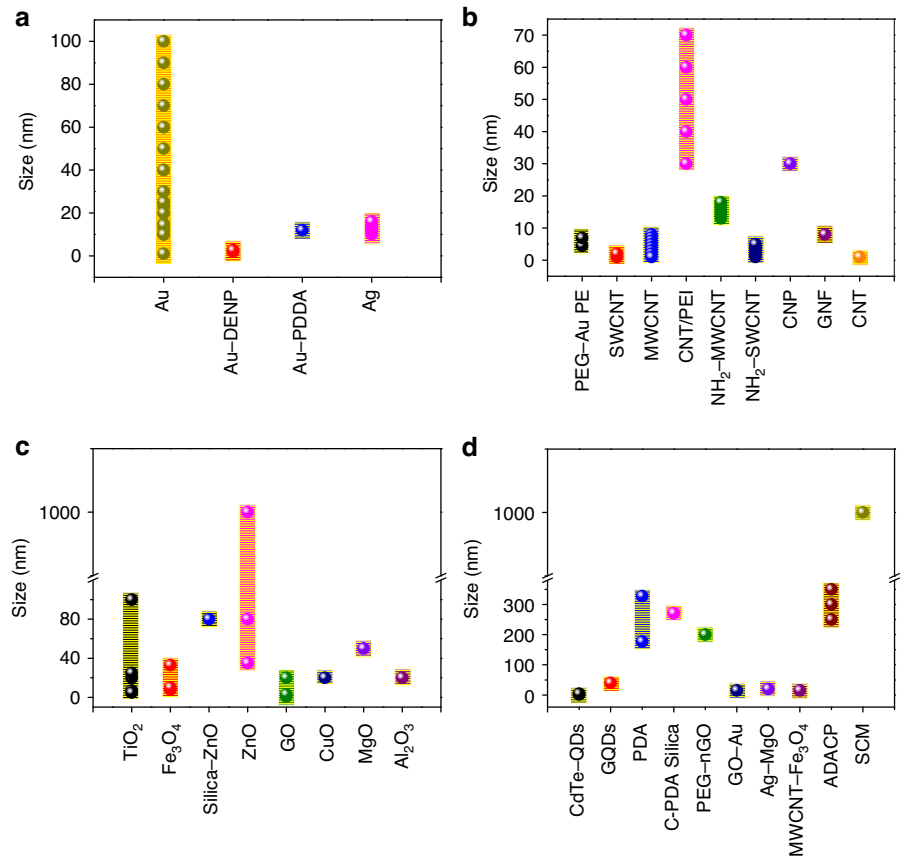

Fig. 4 The size ranges of NPs used in PCR: (**a**) metal NPs, (**b**) carbon-based NPs, (**c**) oxide-based NPs, and (**d**) others

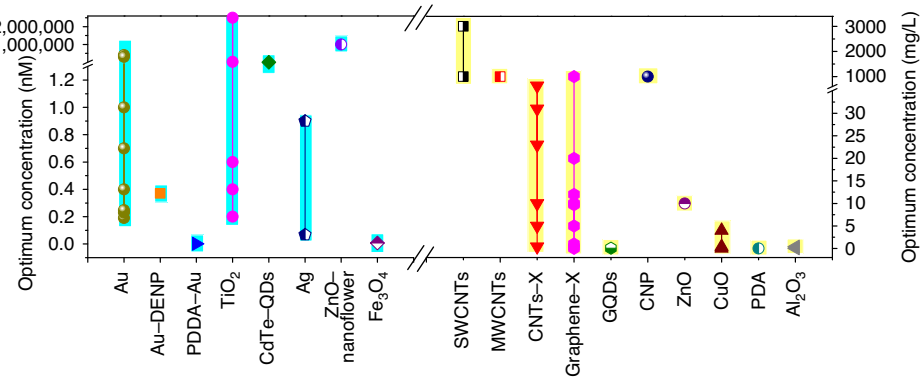

Fig. 5 The optimal concentrations of NPs used in PCR

media: The surface temperature experiences a fast increase, followed by a cooling process. The cooling process of the lattice occurs through phonon-phonon coupling, leading to the dissipation of heat into the surrounding medium of the NP. The LSPR technique is very fast, as it can produce an extremely concentrated area of surface heat within 100 fs[86].

The second way energy is dissipated through processes called non-radiative transitions. These occur when electrons in the excited electronic states in a material decay to lower energy states without the emission of photons. Here, rather than emitting electromagnetic radiation, the energy is radiated out as heat by means of phonon interactions with the nearby atoms or molecules. The

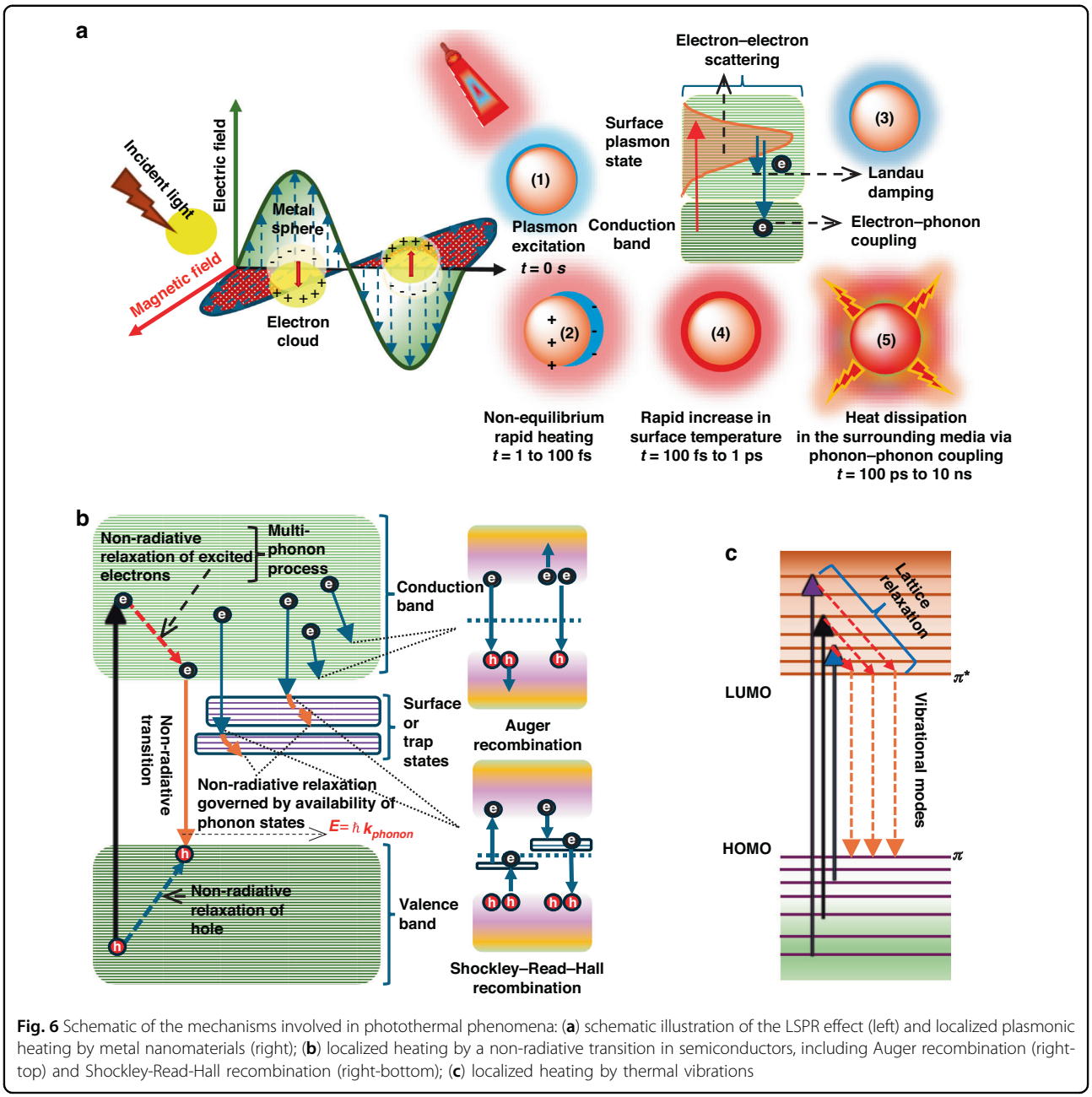

Fig. 6 Schematic of the mechanisms involved in photothermal phenomena: (**a**) schematic illustration of the LSPR effect (left) and localized plasmonic heating by metal nanomaterials (right); (**b**) localized heating by a non-radiative transition in semiconductors, including Auger recombination (right-top) and Shockley-Read-Hall recombination (right-bottom); (**c**) localized heating by thermal vibrations

materials used in semiconductors are mostly linked to this mechanism[87].

Photothermal semiconducting nanomaterials, such as chalcogenides and oxides of metals, governed by this mechanism are also used for heating. These particles are characterized by their bandgap energy, which can be adjusted by manipulating their size, morphology, and surface chemistry[88–90]. By manipulating bandgaps and/or free-carrier-induced LSPRs, the efficiency of light-to-heat transformation conversion in nanomaterials (i.e., semiconductors) can be modulated[56,91,92]. A rise in local lattice temperature can occur when charge carrier recombination in a semiconductor causes the emission of phonons rather than photons, which produces localized heating as depicted in Fig. 6b schematic. Localized heating in semiconductors is principally achieved through two processes: Shockley-Read-Hall and Auger recombination. Auger recombination is an inherent phenomenon that exhibits an upward trend when the bandgaps decrease. Shockley-Read-Hall recombination, defined as a trap-assisted procedure, arises from the existence of defects or impurities within a semiconductor material. When an electron-hole pair undergoes recombination, the absence of photon emission allows for the transfer of energy to either a higher electron in the

conduction band or in the valence band as a deeper hole, as shown in Fig. 6b (right top). In the latter scenario, as illustrated in Fig. 6b (right bottom), electrons of the conduction band first relaxed in the trap level, followed by a transition to the valence band (the place of hole generation). The process of transferring thermal energy is initiated by the simultaneous relaxation of electrons[93,94].

The third mechanism involves the generation of heat through thermal vibrations of atomic lattice primarily associated with the carbon-based nanomaterials[38–40]. The delocalization of electrons in the conjugated and/or hyper-conjugated system facilitates the electron's excitation easily from HOMO (i.e., highest occupied molecular orbital) to LUMO (i.e., lowest unoccupied molecular orbital), thus enabling the absorption of light across a wide spectrum. An electron can elevate from HOMO to LOMO by receiving the matched light energy for its transition (Fig. 6c). A macroscopic increase in the material's temperature occurs due to the relaxation of excited electrons via electron-phonon coupling, which transfers the absorbed light energy to vibrational modes throughout the atomic lattice.

Quantifying light to heat conversion

The capability of NPs to absorb incident light, produce heat, and transfer heat all play essential roles in the optimization of light conversion into heat. The different underlying physical mechanisms for light-to-heat conversion come with different mathematical formulations. Here, we present the most essential formulas for analyzing photothermal conversion regarding light absorption, heat generation, and heat transfer.

Light harvesting

When the surface of a material is subjected to electromagnetic radiation, a part of the photon energy can be absorbed. The light-absorption coefficient of NPs specifies the absorption ability of the incident photon energy. There are two fundamental factors that determine the energy absorbed by NPs: (**1**) the incoming wavelength range for absorption; and (**2**) the absorbance intensity for each wavelength. The total absorptance A (θ) for an incident light with angle (θ) can be defined as Eq. (1) ($\lambda_{\min}$: minimum wavelengths and $\lambda_{\max}$: maximum wavelengths of the incoming light, R (θ, λ): overall light reflectance, T (θ, λ): transmittance power, P (λ) (W/m^2) overall light reflectance at wavelength λ)[95,96].

$$A(\theta) = \frac{\int_{\lambda_{\min}}^{\lambda_{\max}} [1 - R(\theta,\lambda) - T(\theta,\lambda)] P(\theta,\lambda) \mathrm{d}\lambda}{\int_{\lambda_{\min}}^{\lambda_{\max}} P(\lambda) \mathrm{d}\lambda} \quad (1)$$

Accordingly, decreasing the R (θ, λ) and T (θ, λ) results in an increase in light absorption. To achieve high conversion of light-to-heat efficiencies, light absorbers must be able to absorb a broad spectrum of light. The process of light absorption is determined by Beer-Lambert's equation (Eq. (2)), representing an exponential decay having a cumulative behavior ($I = I_0 e^{-kcl}$ (W/m^2): light intensity after the absorption, I_0: light intensity before absorption, k $(M^{-1}\ cm^{-1})$: extinction coefficient, c (M): NPs concentration, l (cm): the optical path length).

$$A = -\ln T = \ln \frac{I_0}{I} \quad (2)$$

By substituting I with $I_0 e^{-kcl}$ in Eq. (2), the absorbance is therefore obtained from $A = kcl$, which depends on the intrinsic properties of the absorber, such as shape, material, and size. However, when we consider employing NPs for heat transfer in a very small volume of medium, mere absorbance consideration is the very macroscopic view. Therefore, we delve deeper to get physical insight into plasmonic heating.

The extinction coefficient depends on the extinction cross section (C_{ext}) of NPs, which is expressed as $C_{ext} = C_{scat} + C_{abs}$, C_{scat}: scattering cross-section, and C_{abs}: absorption cross-section. These two parameters, in turn, can be described in terms of the particle's polarizability (α) of the NPs of radius R due to irradiation with an EM wave by Eqs. (3)–(5) ($\varepsilon(\omega)$: NPs frequency-dependent dielectric constant, ε_m: surrounding medium dielectric constant). Therefore, the dielectric constants and diameter of the NPs, as well as the surrounding medium dielectric constants, are factors affecting the polarizability[97].

$$C_{abs} = \frac{2\pi}{\lambda} Im(\alpha) \quad (3)$$

$$C_{scat} = \frac{8\pi^3}{3\lambda^4} Im(\alpha)^2 \quad (4)$$

$$\alpha(\omega) = 4\pi r R^3 \frac{\varepsilon(\omega) - \varepsilon_m}{\varepsilon(\omega) + 2\varepsilon_m} \quad (5)$$

As described in Eq. (6), by considering the relationship between the heat power (Q) produced by NPs when exposed to an EM wave at a certain intensity (I_o), the importance of C_{abs} can be comprehended[98]:

$$C_{abs} = \frac{Q}{I_o} \quad (6)$$

Hence, at a certain EM wavelength, the heat generated by the NPs is directly proportional to their absorption cross-section.

In addition to the above discussion, we demonstrate the connection between light and NPs and the generation of heat through the Joule effect. The formula for the time-averaged heat power density q is provided below (J: electronic current density, E: electric field inside the NPs)[99]:

$$q = \frac{1}{2} Re\{J \,.\, E^*\} \tag{7}$$

Using the relation between the polarization vector (P) and E; $J = \partial P/\partial t$ and $P = \varepsilon_o(\varepsilon - 1)$, for a monochromatic light of angular frequency (ω) can be expressed as: $q = \frac{\omega}{2}\varepsilon_o Im\{\varepsilon\}|E|^2$. The heat power density within a NP is directly proportional to the square of the amplitude of the electric field. Poynting's theorem states that the total heat power (Q) emitted by a NP may be calculated by integrating q over its volume (V).

$$Q = \frac{\omega}{2}\varepsilon_o Im\{\varepsilon\} \iiint |E|^2 dV \tag{8}$$

The heat produced by a NP causes the temperature to rise in both the NP and its surrounding media as a result of heat diffusion. This can be expressed using the widely recognized general heat transfer Eq. (9) (ρ: the material's density, Cp: specific heat capacity, T(r): absolute temperature, κ: surrounding medium thermal conductivity).

$$\rho C_p \frac{\partial T(r)}{\partial t} = \nabla.[k\,\nabla T(r)] + Q \tag{9}$$

Conversion efficiency of light-to-heat

The photothermal conversion efficiency (η) is an important factor in quantifying the absorbed energy converted to heat for different plasmonic nanostructures. This parameter can be expressed as Eq. (10) (Q_T: total heat energy produced by the NPs, E_T: total energy output of the incoming light, m (kg): mass of the NPs, c (J/kgK): specific heat capacity, ΔT (K): temperature change of the NPs during the radiation time (t (s)), p: power, A (m^2): surface area of the incoming light)[100,101].

$$\eta = \frac{Q_T}{E_T} = \frac{mc\triangle T}{pAt} \tag{10}$$

In this procedure, to measure η, the entire incident light is considered for input energy. However, from the absorbed, scattered, reflected, and transmitted photons, only the absorbed photons have the ability to convert the energy (light to heat).

Moreover, as in this strategy, the transfer of heat from the photothermal material to the surroundings is not considered, which doesn't solve the problem of heating a small volume of medium. So, the photothermal conversion efficiency η can be estimated by writing the heat balance equation[102]:

$$\sum mC_p \frac{dT}{dt} = Q_{NP} + Q_{solvent} - Q_{ext} \tag{11}$$

$\sum mC_p$: summation of mass and heat capacities of all NPs,

$\frac{dT}{dt}$: temperature increase rate,

Q_{ext}: external heat flux,

$Q_{NP} + Q_{solvent}$: heat produced by converting the absorbed light into heat by either NPs (Q_{NP}) or by the solvent ($Q_{solvent}$).

Estimating the heat loss to the media causes the temperature decay process once the incident light is removed. The Q_{NP} is defined using Eq. (12) in the switched-OFF light mode:

$$Q_{NP} = I_o(1 - 10^{-A_\lambda})\eta \tag{12}$$

where A_λ is the absorbance at irradiation wavelength λ. In equilibrium conditions, $\sum mC_p \frac{dT}{dt} = 0$ and η can be calculated as Eqs. (13)–(15) (Q_{ext}: computable from experimental cooling kinetics, h: NPs' heat transfer coefficient, A: for heat transfer surface area to surrounding media, T_{amb}: surroundings temperature, and T: current temperature).

$$\eta = \frac{Q_{ext} - Q_{solvent}}{I_o(1 - 10^{-A_\lambda})} \tag{13}$$

$$= \frac{hA(T_{\max} - T_{amb}) - Q_{solvent}}{I_o\left(1 - 10^{-A_\lambda}\right)} \tag{14}$$

$$= \frac{\sum mC_p(T_{\max} - T_{amb}) - Q_{solvent}}{\tau_c I_o\left(1 - 10^{-A_\lambda}\right)} \tag{15}$$

The actual temperature equals the steady-state temperature $T = T_{\max} = T_{amb} + \Delta T$ at equilibrium. These parameters can be estimated using the product of m and C_p and the cooling time coefficient (τ_c), of all the NPs. The absolute value of η will be influenced by a number of experimental circumstances. For example, factors that may significantly influence the determination of τc, the method of actual temperature measurement, will impact the sum of the product of mass and heat capacity.

Heat transfer

Another underlying part of the light-to-heat conversion is heat transfer, which is conducted by conduction, convection, and radiation mechanisms[95,103]. Heat conduction is the process of transferring heat from a warmer area to a cooler one. The heat conduction can be calculated as Eq.

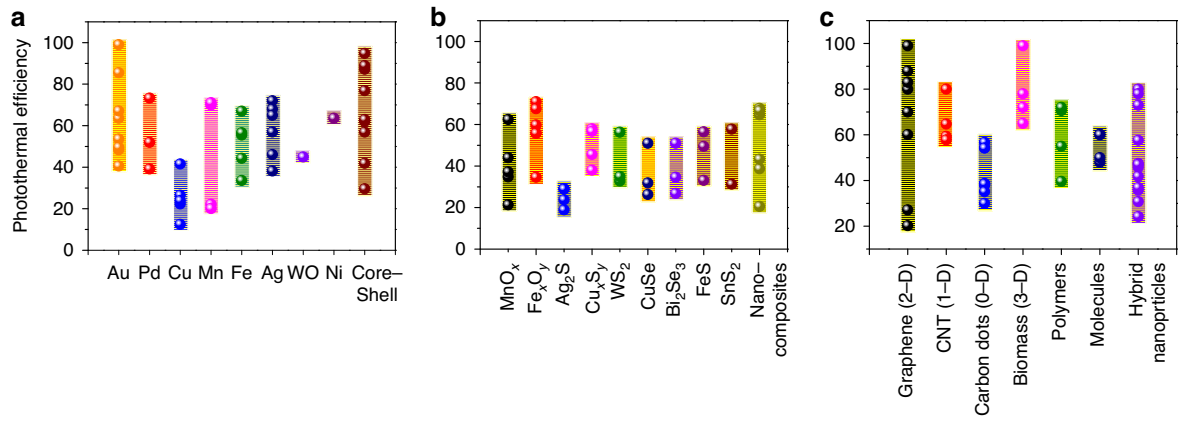

Fig. 7 Photothermal conversion by nanomaterials in biological applications: (**a**) photothermal efficiency of metal nanomaterials, including Au[148–151,261–264], Pd[265–268], Cu[269–273], Mn[274–277], Fe[278–282], Ag[264,283–287], WO[288], Ni[289], and core-shell structures[153,290–297]; (**b**) photothermal efficiency of semiconductor nanomaterials, including MnO_x[298–302], Fe_xO_y[303–308], Ag_2S[309–312], CuS[313–316], WS_2[317–319], CuSe[320–322], $BiSe_3$[323–325], FeS[326–328], SnS_2[329,330], and nanocomposites[331–336]; (**c**) photothermal efficiency of carbon nanostructures, molecules, and polymers, including graphene and derivatives[163,164,337–342], CNT[343–345], carbon dots[346–352], biomass[155,353–355], polymers[356–359], molecules[360–363], and hybrid NPs[364–375]

(16) (k_{NP} (W/mK): NPs' thermal conductivity, d (m): light absorber thickness).

$$Q_{conduction} = k_{NP} A \frac{(T_{\max} - T_{amb})}{d} \quad (16)$$

Thermal convection involves the movement of a mass of fluid from the heating source into a cooler part of the fluid. In this way, heat transfer is caused by temperature variations within the fluid, and it is given as:

$$Q_{convection} = hA(T_{\max} - T_{amb}) \quad (17)$$

Lastly, thermal radiation refers to the radiation of EM waves by all objects without the need for any media. The Stefan-Boltzmann Law can be expressed for energy exchange between two regions with different temperatures as:

$$Q_{radiation} = \epsilon\, \sigma A\, (T_{\max}{}^4 - T_{amb}{}^4) \quad (18)$$

where ϵ represents the radiation coefficient, σ is Stefan's coefficient $(5.6703 \times 10^8 \quad Wm^{-2}K^{-4})$; consequently, besides the physical characteristics of the NPs, their surrounding medium also affects the heat transfer. So, the conversion of light to heat can be improved by the appropriate selection of NPs and considering the condition of their surrounding medium.

Developments of Photothermal Nanomaterials

The application of a photothermal process starts with the selection of particular NPs. The principal phenomena governing this process are fundamentally different: metal NPs display the LSPR effect[35,104], intrinsic semiconductors and lightly doped semiconductors show non-radiative relaxation[91,92], and carbon nanostructures, including polymers, demonstrate thermal vibration-based heating assisted by the delocalization of π electron clouds[105,106]. However, this bifurcation is not sacrosanct, and even highly doped semiconductors can reveal LSPR[56]. Similarly, 2D materials can unveil the coupling of both LSPR and non-radiative relaxation[107]. Extensive research has been done to show the efficacy of an array of nanomaterials and compare them for their suitability as photothermal converters for applications in nucleic acid amplification in PCR[108–112], sensors[113–120], biomedica[86,111,121,122], bioimaging[123–125], superhydrophobic coating[126,127], immunomagnetic bioassays[128], optical nanothermometry[129], atomic switches[130], spectroscopy[122,131], nanofabrication[132,133], acoustic wave detection[134], seawater desalination[135,136], plasmonic photocatalysis[137,138], strain modulation[139], and plasmonic actuation[140]. Figure 7a–c graphically reviews some of the latest works and compare the photothermal conversion efficiency on metals, semiconductors, and carbon NPs, respectively.

A wide range of photothermal efficiencies is exhibited by the nanomaterials that significantly depend upon their size and/or morphology. These distinctions were clearly observed in several reports. The amplitude of the electron oscillation of Au nanospheres rises with an increase in particle size that shifts the LSPR towards the lower energy side and eventually controls the localized heating[141,142]. Apart from size, the morphology of Au NPs exhibits a vital role in modifying the LSPR energy; these structural variations include preparing them into nanorods[143,144], nanostars[145], or nanoshells[146,147]. The latter is manifested by the photothermal efficiency of Au hollow rods, with an efficiency of about 99%[148], whereas Au nanospheres and Au nanorods exhibited efficiencies of 54% and 41%,

respectively[149–151]. The phenomenon of reabsorption has been proposed as a possible explanation for such high efficiency in hollow rods[148,152]. Moreover, there are also reports for core-shell structure; for example, when Au is combined with Ag in Ag core@Au shell, it showed a photothermal efficiency of 87.2%[153]. Though the efficiency of such a structure is less than the maximum reported, it gives various applications a range of efficiencies. It is apparent that photothermal efficiency changes not only with the change of materials but also with morphology and size. The effect of size and morphology on photothermal efficiency was meticulously tabulated by Zhuoqian et al.[154]. Photothermal efficiency is similarly tunable in semiconductor and carbon-based photothermal nanomaterials, as shown in Fig. 7b, c. Importantly, from the comparison in Fig. 7, carbon nanostructures, molecules, and polymers are not far behind metals in photothermal efficiency. In some cases, biomass precursor-based carbon nanostructures showed similar efficiency in generating heat for solar water evaporation to their metal counterparts, such as 99% in PPy decorated cattail fiber (CF) foam[155]. This is a promising development, as cattail fiber is an aquatic plant that can spread swiftly and provide abundant biomass lignocellulose. Based on this summary of various nanomaterials as photothermal converters, selecting the materials for advanced applications becomes easier.

In this work, we focus on the selection of NPs for nucleic acid amplification in PCR. For this application, we are specifically interested in controlling the heating rate and cooling rate and the time required to complete the total number of thermal cycles before a positive result can be reported. For ultrafast thermocycling using nanomaterials, the NPs' material type, size, and morphology are key, and they have been well-documented over the last decade[156]. Efficient photothermal conversion can be achieved by tuning the LSPR to the desired spectral window in the case of metals. Similarly, in order to control the non-radiative relaxation in semiconductor particles, the band gap and charge trapping states can again be tuned by size and shape[157–160]. In Table 3, the performance of a set of nanomaterials for use in PCR is compared. Au NP-based thermal cycling remains the most popular choice among researchers and manufacturers. Nevertheless, the volatile thermodynamic characteristics of Au nanorods at elevated temperatures render them inappropriate as constituents for continuous heat-transfer agents, hence posing a significant obstacle to Au NP-based PCR. Noble metal nanostructure-based thermal cycling has been reported so far to be accomplished within 1200 seconds to 54 seconds with Au nanorods[161,162].

On the other hand, semiconductors exhibit resistance to elevated temperatures due to their inherent thermal stability and offer a certain degree of advantage in terms of thermal stability. However, semiconductor-based thermal cycling is found to be time-consuming compared to its counterpart metal and carbon nanostructures. In order to

Table 3 Different types of NPs, their optimum concentrations, effects, mechanisms, and applications for enhancing PCR

Mechanism	Materials and structure	Dimension	No. of thermal cycles	Heating rate (° C/s)	Cooling rate (° C/s)	Time (s)	References
Plasmonic localized heating in metals	Au nanosphere	*D*: 60 nm	30	7.62	3.33	700	253
	Au Nanorod	*D*: 10 nm *L*: 41 nm	30	72	50	54	162
	Au Nanorod	–	30	6.25	1.99	1200	161
	Au bipyramid	–	30	16.6	9.4	142	254
	SiO_2Au Fe_2O_3 Core-Shell	–	30	7.69	5.89	1200	255
	Au nanorod		45	6.7	4.7	900	256
	Au nanoshell	Total Dia: 155 ± 7 nm Core Dia: 121 ± 5 nm	40	2.4 ± 0.049	3.9 ± 0.052	800	257
Non-radiative relaxation in semiconductors	Fe_3O_4 nanocluster	10 to 11nm cubic nanocrystals	40	4.5	2.25	600	258
	ZnO nanoflower	–	–	–	–	70 min	248
Thermal vibrations of molecules	CNT, GO, and rGO	–	40	22	23.5	300	259
	Carbon black		30	22	2.6	420	260

achieve photothermal cyclers using cost-effective and easily expandable materials, electron-rich carbon nanostructures are a suitable alternative to noble metals. This occurs because the interaction between incoming photons and the numerous π electrons in the conjugated system considerably leads to thermal energy dissipation. The incoming photons trigger electronic transitions and induce resonance in the oscillation of π electron clouds. This leads to vibrational changes, which help electrons and phonons as well as phonon interactions within the carbon nanomaterial. Hence, this enhances the formation of electron-phonon pairs and ultimately improves photothermal conversion efficiency through thermal vibrations[163–167]. Moreover, the carbon nanostructure-based PCR has a significantly comparable thermal cycling time with metals and is better than the semiconductor shown in Table 3. Though carbon-based photothermal materials exhibit high photothermal conversion efficiencies comparable to metallic counterparts and better than semiconductor NPs. However, Au NP-based thermal cycling continues to be the preferred option for researchers and manufacturers. Nonetheless, the compatibility of carbon-based thermal cycling remains in its nascent phase for integration with the current PCR. The predominant rationale for the majority of documented work on thermal cycling is the utilization of Au NPs, recognized for their tunable plasmonic and biocompatibility. Therefore, selecting materials for PCR applications not only focuses on the photothermal conversion efficiency but also needs a holistic approach that converges all the parameters to achieve ultrafast diagnostic devices.

Beyond the traditional materials documented thus far for applications in photothermal energy conversion, there exists a novel class of emerging materials that holds significant promise for utilization as thermoplasmonic materials. Within the framework of plasmonic science and engineering, the use of artificially engineered materials and metamaterials has been proposed. The use of artificially engineered materials has been explored since the 1940s and 1950s in order to emulate effective media parameters following Drude-Lorentz models, applicable to radar lenses, refractive index variations, or delay lines, among others[168–170]. Further on, Victor Veselago[171] studied the theoretical properties of materials that could have any combination of values of effective ε and μ, either positive or negative, leading to double negative ε and μ materials, not encountered in nature. These materials exhibit unusual properties such as anti-parallel phase and group velocity (for which these materials are also called Left Handed Materials, LHM, in contrast to conventional materials), inversion of Snell's law, and inversion of Cerenkov radiation, among others. However, these new artificial materials, termed metamaterials, aren't readily available in nature, so they must be artificially engineered, with the first practical implementations within the microwave spectrum proposed in the early 2000s[172]. From that point, a relevant amount of results related to metamaterials has been reported, in which multiple frequency bands from acoustics up to UV and different application domains[173,174]. Among the different metamaterial configurations, 2D metasurfaces and 3D configurations (mainly based on 2D structure stacking) have attracted attention, owing to their flexibility to be employed in order to enhance sensing capabilities, improve stealthing, or provide agile communication systems, to name a few[175–177]. In relation to plasmonics, metamaterials have been employed in order to enhance detection mainly by increasing field values aided by inherent lensing and focusing properties, for example, in chiral media[178], controlling light intensity and polarization in molecular plasmonics[179], or nanochemistry applications[180]. Taking advantage of the capability of adapting the 2D/2D stacking configurations of artificially engineered structures, such as layers of discs, rods, or resonant structures, the aforementioned field enhancement properties of metamaterials/metasurfaces have also been explored in relation to thermoplasmonics. A broadband solar light absorber based on Cu metal nanostructure fabricated on the surface of a Palash leaf aided by pulsed layer deposition is described in[181]. The use of nanoholes within metal structures is analyzed in[182], in terms of practical variations in hole diameter as well as metal layer thickness and non-ideal conditions given by material properties and/or fabrication process. Advances in the use of thermoplasmonic and photothermal metamaterials in the field of solar energy are described in[183], including photonic crystal–based thermal emitter technology, the use of rare earth ion–doped luminescent materials or rare earth ion–doped glass emitters, and semiconductor emitters with plasmonic nanogratings, among others. Hyperbolic metamaterials within the NIR-II and NIR-III are described in[184], providing higher temperature increases as compared to conventional Au nano-disk configurations for application within biomedical diagnostics. Dynamic control of metasurface properties within the optical domain is proposed in[185], aided by the use of liquid crystal technology, within the 750–770 nm wavelength region.

Microfluidic-based PCR using light-to-heat conversion

Microfluidic platforms as miniaturized devices have been employed to integrate several laboratory functions on a single chip and manipulate small volumes of fluids in microchannels[186,187]. Microfluidic-based technologies offer numerous advantages, such as minimal sample requirements, inexpensive fabrication, adaptability, shortened analysis time, portability, and automation[188,189]. However, at the microscale level, microfluidics has some

drawbacks, where capillary forces, surface roughness, and chemical interactions between materials can become more significant[190,191]. This might lead to experimental complications that are uncommon with traditional lab equipment. Furthermore, due to the small scale of microfluidic devices, the signals generated are typically very small, and the background noise can be relatively high[192,193]. This can make distinguishing a signal from the noise challenging, resulting in inaccurate measurements. Consequently, to enhance the signal-to-noise ratio and ensure accuracy, optimizing microfluidic devices and detection methods is crucial[194]. Despite these challenges, microfluidics is becoming more popular worldwide, with the increasing demand for portable, easy-to-use point-of-care (POC), and compact devices that can perform more rapid and affordable diagnostic testing[195,196]. Scientists have recently shown great interest in integrating microfluidic systems with PCR techniques using light-to-heat conversion for biology applications to recognize viruses and bacterial diseases through the amplification of pathogen molecules[110,197,198]. They used light-emitting diodes (LEDs) as heat sources in microfluid-based PCR techniques because of their fast heat transfer properties, low power consumption, and affordable price[110].

A remarkable achievement using an ultrafast photonic PCR thermal cycler was demonstrated, in which 30 thermal cycles were completed within 5 min with an ultrafast heating rate of 12.79 °C/s and a cooling rate of 6.6 °C/s[110]. This was made possible by combining a 120 nm-thick Au film, which served as a converter of light to heat, and LEDs with a power intensity of only 3.5 W, as the source of heat (Fig. 8a). The thin Au film used in the experiment was found to have an impressive light absorption rate of 65% and the ability to rapidly heat the surrounding medium to 150 °C within just 3 min. While properties such as low power intensity, high-speed thermal cycling, and the ability for easy incorporation into existing systems made this method a promising candidate for POC diagnostic applications, its relatively low amplification efficiency, which was based on the non-uniform temperature distribution under a single two-dimensional heater, needed to be improved. Lee et al. utilized an LED-driven optical cavity with two thin Au films with different thicknesses (120/10 nm for the top/bottom film) to provide a more uniform temperature distribution during PCR thermal cycling (Fig. 8b)[197]. According to the results, the temperature distribution of the PCR reagents became effectively uniform, with a difference of 1.9/0.2 °C at temperatures of 94/60 °C. Additionally, 30 thermal cycles were rapidly completed within only 4–10 min for different sample volumes of 1.3–10 μL. Furthermore, this method successfully amplified nucleic acids (c-MET cDNA), even at low concentrations of 10^{-8} ng/μL, by 40 cycles of cavity PCR. This remarkable efficiency was achieved within a short time frame of 15 min, highlighting the method's potential as a fast and reliable solution for nucleic acid amplification. Subsequently, they employed a combination of three techniques on a chip, including filtering, lysis, and PCR, for rapidly identifying bacterial pathogens in urine samples (Fig. 8c)[198]. The nanoporous membranes coated with titanium (Ti) (5 nm) and Au (80 nm) utilized in this platform have a dual function: they not only concentrate bacteria but also function as a photothermal actuator. Two LEDs with $\lambda = 447.5$ nm and P = 890 mW were employed for measuring temperature and testing the *E. coli* bacteria in the sample. With remarkable efficiency, this system achieved bacterial enrichment of up to 40,000-fold within just 2 min, with a capture efficiency rate of over 90%. It also provided on-site photothermal lysing and initial denaturation in just 3 min, followed by nucleic acid amplification within a further 10 min. Finally, bacterial pathogens in urine samples were detected in less than 20 min. They successfully detected bacteria at low concentrations (10^3 CFU/mL) using this nanophotonic PCR system. However, in comparison with a traditional benchtop thermocycler, their system resulted in a lower intensity of the specific band (the desired DNA fragment size). They proposed that this difference in DNA amplification efficiency may stem from the fact that their system relies on a two-stage fast thermocycling method, which can potentially result in a lower amplification efficiency compared to a more traditional three-step thermocycling method commonly used in benchtop thermocyclers. Similarly, Lee et al. demonstrated strong laser energy absorption by the Au-deposited glass fiber membranes (Fig. 8d)[199]. Glass fibers were selected for the study due to their superior absorption capacity over other materials, and the study also investigated mixed-matrix membranes, nitrocellulose, polyether sulfone, and vivid plasma membranes with an area of 4 mm^2. Using 25 rapid thermal cycles between the solution temperatures of 63 °C and 95 °C, PCR was completed in 6 min. Next, in 12 min, the amplified samples on the membrane were successfully examined using SYBR fluorescent signal assessment. In another study, a thin 120-nm-thick Au film deposited on a PMMA substrate was employed to act as the PCR reaction's heating source[200]. Non-homogeneous temperature distribution in the reaction chamber is one of the primary disadvantages of certain plasmonic PCR thermal cyclers, particularly those that utilize a plasmonic film instead of plasmonic NPs. Therefore, they added TiO_2 NP suspensions, with a 0.4 nM optimal concentration to solve the problem of the chamber's non-homogeneous temperature by improving the sample's thermal conductivity. A 10 W blue LED with a peak wavelength of 447.5 nm and a thermoelectric cooler (Peltier) module make up the thermal cycler's heating and cooling components, respectively. The rates of cooling and heating are 2.65 °C/s

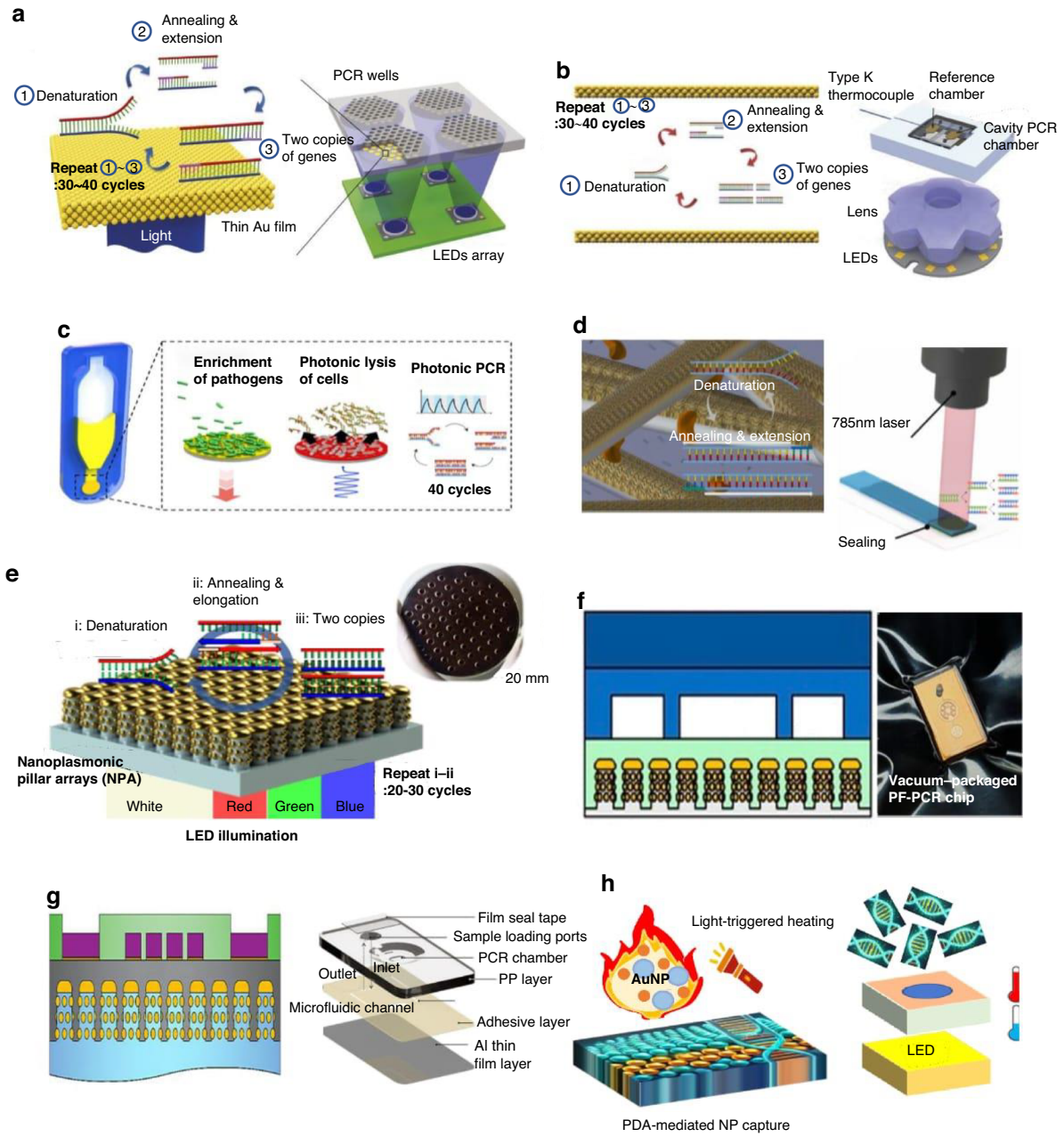

Fig. 8 Photonic thermocycler with (**a**) a light-to-heat converter comprised of a thin Au film. Reprinted from ref. [110], with permission from Springer Nature; (**b**) an LED-based system that incorporates two thin Au films into an optical cavity. Reprinted from ref. [197], with permission from John Wiley and Sons; (**c**) an Au-coated nanoporous membrane. Reprinted from ref. [198], with permission from the American Chemical Society; (**d**) Au-deposited glass fiber membranes. Reprinted with permission from ref. [199]. Copyright 2022 Elsevier; (**e**) a microfluidic chip made by joining the HSQ-coated PNAs substrate to the polydimethylsiloxane (PDMS). Reprinted from ref. [201], with permission from the American Chemical Society; (**f**) a microfluidic chip made by joining the HSQ-coated PNAs substrate to the bilayered PDMS. Reprinted from[202], available under Attribution CC BY-NC-ND 4.0; (**g**) a plastic-on-metal (PoM) thin film cartridge made by joining the SiO_2-coated PNAs substrate to the Al thin film layer. Reprinted from ref. [203], available under Attribution CC BY-NC-ND 4.0; (**h**) an Au NP coating using PDA[204]

and 4.44 °C/s, respectively. In 2020, plasmonic nanopillar arrays (PNAs) were employed for a rapid diagnostics system (Fig. 8e)[201]. The PNAs consist of Au nanoislands with nanogaps on glass nanopillar arrays (GNAs). In this study, 500 nm thick hydrogen silsesquioxane (HSQ) resin was spin-coated onto the PNAs to create a passivation layer. Since electrically charged Au nanoislands disrupt the reaction by attracting PCR components like Taq

polymerase, the HSQ layer acts as a dielectric passivation layer to stop the PCR reaction from being inhibited. They were able to perform 30 thermal cycles between 98 °C and 60 °C in 3 min and 30 s using a single white LED light as an excitation source. The nanoplasmonic PCR chip has also demonstrated the rapid amplification of λ-DNA with an initial concentration of 0.1 ng/μL in 20 cycles and complementary DNA (cDNA) with an initial concentration of 0.1 ng/μL in 30 thermal cycles. The PNAs demonstrate remarkable light absorption with a 2.3-times increase compared to a thin Au film when exposed to white LED illumination. Similarly, GNAs containing Au nanoislands were coated by HSQ for an ultrafast PCR (Fig. 8f)[202]. They obtained a 91% amplification efficiency, a heating rate of 11.95 °C/s, and a cooling rate of 7.31 °C/s. In contrast to traditional benchtop qPCR systems, the overall run time of this system is around 12 times quicker for 40 cycles of PCR. In another study, after the creation of nanoisland masks and the formation of nanoplasmonic substrate (NPS) by heat evaporation of an Au layer (40 nm) covering the GNAs' top and sidewalls, silicon dioxide (SiO_2) with a thickness of 500 nm was applied to reduce the surface roughness (Fig. 8g)[203]. They employed a plastic-on-metal (PoM) thin film cartridge that consists of an aluminum (Al) thin film layer, an adhesive layer, and a polypropylene (PP) layer to improve the heat transition and the real-time quantification without any spectral crosstalk during the plasmonic thermocycling. In this study, the heating and cooling rates of the Al thin film were 2.9 and 3.2 times faster than those of the plastic-on-glass (PoG) cartridge, respectively, with a ramping-up rate of 18.85 °C/s and a ramping-down rate of 8.89 °C/s. This system facilitated rapid molecular diagnosis of COVID-19 within just 10 min, incorporating a 210-second RT process and a 400-second amplification process for 40 PCR cycles. This system exhibited high amplification efficiency (over 95%), high classification accuracy (over 95%), and high total percent agreement of clinical tests (over 90%). In 2024, after coating polycarbonate (PC) with PDA, PEI was bonded to the substrate to trap the citrate-capped Au NPs that are negatively charged (Fig. 8h)[204]. Afterward, the surface coated with PDA, PEI, and Au NPs was then electrolessly deposited with Au. Next, a closed-chamber PCR chip was used to successfully amplify a target by employing a white LED. Using the PDA-mediated technique for coating in this study, the reaction time was 12 min to replicate 34 PCR cycles.

Table 4 compares papers that employed a plasmonic mechanism for PCR reactions in microfluidics. Au nanoislands applied to glass pillars show outstanding photothermal efficiency and extensive absorption in visible light areas. It has also shown a significant increase in both the heating and cooling rates with the maximum values of 18.85 °C/s and 12.4 °C/s, respectively.

Table 4 Characteristics of photonic thermocyclers on microfluidic systems

Plasmonic nanomaterials	Reaction volume	No. of thermal cycles	Heating rate (°C/s)	Cooling rate (°C/s)	Heating power	Sensitivity	Time (s)	Refs.
120-nm-thick Au film	10 µL	30	12.79	6.6	≈3 W	0.1 ng/µL	Less than 300	110
10/120-nm-thick Au films	1.3–10 µL	30	7.5	6.35	≈20 W	2 copies/µL	240-600	197
Au-coated nanoporous membrane	20 µL	40	–	–	0.75 W	1000 CFU/mL	600	198
Au-coated fiber glass membranes	20 µL	25	–	–	1.23 W	–	360	199
PMMA covered with a 120 nm-thick Au layer/ TiO2 NPs	20 µL	45	4.44	2.65	10 w	–	4000	200
HSQ-coated PNAs	15 µL	30	9.3	12.4	–	0.1 ng/µL	210	201
HSQ-coated PNAs	20 µL	40	11.95	7.31	–	9.55×10^4 copies/µL	264	202
SiO_2-coated PNAs	15 µL	40	18.85	8.89	–	20 copies/2µL	400	203
PDA-PEI-Au NP-ELD	20 µL (off-chip) 8 µL (on-chip)	34	~9.5	~8.89	4 w	8 copies/µL	720	204

Nevertheless, the Au layers in these investigations were created utilizing costly equipment-intensive physical deposition methods (electron beam evaporation or thermal evaporation). The Au NP coating using PDA is more applicable in a wider range of scenarios because it does not require costly equipment, unlike physical deposition approaches.

Conclusion

In summary, we presented a detailed review of nanoPCR, photothermal PCR, and on-chip photothermal PCR applications. The PCR system has incorporated various classes of nanomaterials to date, significantly reducing reaction time, expanding the annealing temperature range, increasing product yield and amplification efficiency, enhancing detection sensitivity, reducing non-specific products, and improving the detection rate. For instance, Au NPs with size ranges of 1-100 nm are the most commonly used metal NPs in PCR. They were found to have a sensitivity up to 1000-fold greater than conventional PCR. The maximum optimal concentration of Au NP used in the PCR process is 0.4 mM. They could enhance the detection rate to approximately 77%. Studies have shown that TiO_2-based nanoPCRs, at optimal concentrations of 0.2 g/L and 0.4 nM, can significantly reduce the overall PCR time by up to 50%. Introducing SWCNTs and MWCNTs with an optimal concentration of 1 g/L to PCR reagents was determined to be a suitable option to increase the efficiency and specificity of long PCR (14.3 kb). SWCNTs were also found to increase the PCR yield with an optimal concentration of 3 g/L. Fe_3O_4 NPs with a very low optimal concentration of 0.72×10^{-2} nM were reported to result in a 190% increase in the PCR yield compared to the PCR reaction without NPs. ZnO nanoflowers and SCM are another type of NP, characterized by a larger size (1 μm), which increase the sensitivity and specificity of the PCR process. The unique photothermal properties of NPs and their physicochemical properties can enable scientists to progress in robust, portable, and ultrafast PCR at the POC level. To date, NPs such as metals, semiconductors, and carbons have demonstrated different ranges of photothermal efficiencies for various applications based on their materials, morphology, and size. Using plasmonic localized heating in metals, non-radiative relaxation in semiconductors, and thermal vibration of carbon molecules, PCR applications have achieved rapid and efficient amplifications. Considering the heating rate, cooling rate, and total PCR time as main factors in PCR, the Au nanorod with dimensions of $D = 10$ nm and $L = 41$ nm is better than the rest with a significant margin. Besides, carbon nanostructure-based PCRs perform better than semiconductors in terms of thermal cycling time. Microfluidics-based PCRs have utilized certain metallic NPs to take advantage of plasmonic -controlled heating. Nevertheless, the extensive capacity for effective conversion of light into heat and the utilization of NPs in PCR remain largely untapped. This is an opportunity to enhance the microfluidic PCR by including a wide range of advanced nanomaterials, thereby satisfying the need for the development of ultrafast PCR.

Microfluidics-based PCRs have recently utilized only a limited number of metals with plasmonic localized heating. Despite the advantages of light-to-heat conversion and the photothermal efficiencies of NPs, only a limited number of devices use light-to-heat conversion in microfluidics systems. Integrating photothermal effects and microfluidic fields for PCR will be essential to overcome existing challenges. Most of the applications are adopted with Au NPs for thermal cycling, but we have observed that even carbon NPs have shown a significant photothermal conversion efficiency, and they are biocompatible, easy to fabricate, and inexpensive. These attributes suggest that the application of carbon-based nanomaterials could be of potential advantage for thermal cycling in the future. In order to immobilize and create metal NPs that allow photothermal heating of surfaces, intermediate layers can be substituted for expensive, equipment-intensive physical deposition techniques like thermal evaporation or electron beam evaporation, which are not accessible to all researchers.

Acknowledgements

Figure 3 was created with Biorender.com. M.M. and his PhD student (S.S.) acknowledge funding from CONACYT through a doctoral scholarship. M.M. acknowledges the funding provided by CONAHCYT in the form of a scholarship as a member of the National System of Researchers (CVU:969467) and the financial support of the FEMSA foundation.

Author details

[1]School of Engineering and Sciences, Tecnologico de Monterrey, Monterrey 64849 NL, Mexico. [2]Department of Electrical, Electronic and Communication Engineering and the Institute of Smart Cities, Public University of Navarre (UPNA), 31006 Pamplona, Spain. [3]Research Lab for Advanced Separation Processes, Department of Chemical Engineering, Iran University of Science and Technology, Narmak, Tehran 16846-13114, Iran. [4]Department of Mechanical and Aerospace Engineering, University of California Irvine, Irvine, CA 92697, USA

Author contributions

S.S., A.B.S., M.M., V.K., and L.V. Wrote the initial draft of the manuscript. M.M., M.J.M., M.R., and S.N.A. edited the manuscript. M.M. supervised the whole work. All authors have read and agreed to the published version of the manuscript.

Conflict of interest

The authors declare no competing interests.

Received: 7 October 2024 Revised: 8 January 2025 Accepted: 14 January 2025
Published online: 19 June 2025

References

1. Elizaquível, P., Aznar, R. & Sánchez, G. Recent developments in the use of viability dyes and quantitative PCR in the food microbiology field. *J. Appl. Microbiol.* **116**, 1–13 (2014).

2. Kuypers, J. & Jerome, K. R. Applications of digital PCR for clinical microbiology. *J. Clin. Microbiol.* **55**, 1621–1628 (2017).
3. Matheson, C. D. et al. Removal of metal ion inhibition encountered during DNA extraction and amplification of copper-preserved archaeological bone using size exclusion chromatography. *Am. J. Phys. Anthropol.* **140**, 384–391 (2009).
4. Singh, J., Birbian, N., Sinha, S. & Goswami, A. A critical review on PCR, its types and applications. *Int. J. Adv. Res. Biol. Sci.* **1**, 65–80 (2014).
5. Madadelahi, M., Agarwal, R., Martinez-Chapa, S. O. & Madou, M. J. A roadmap to high-speed polymerase chain reaction (PCR): COVID-19 as a technology accelerator. *Biosens. Bioelectron.* **246**, 115830 (2023).
6. Vajpayee, K., Dash, H. R., Parekh, P. B. & Shukla, R. K. PCR inhibitors and facilitators—their role in forensic DNA analysis. *Forensic Sci. Int.* **349**, 111773 (2023).
7. Akane, A. et al. Purification of forensic specimens for the polymerase chain reaction (PCR) analysis. *J. Forensic Sci.* **38**, 691–701 (1993).
8. Al-Soud, W. A. & Radstrom, P. Purification and characterization of PCR-inhibitory components in blood cells. *J. Clin. Microbiol.* **39**, 485–493 (2001).
9. Al-Soud, W. A., Jönsson, L. J. & Rådström, P. Identification and characterization of im- munoglobulin G in blood as a major inhibitor of diagnostic PCR. *J. Clin. Microbiol.* **38**, 345–350 (2000).
10. Eckhart, L., Bach, J., Ban, J. & Tschachler, E. Melanin binds reversibly to thermostable DNA polymerase and inhibits its activity. *Biochem. Biophys. Res. Commun.* **271**, 726–730 (2000).
11. Yoshii, T., Tamura, K., Taniguchi, T., Akiyama, K. & Ishiyama, I. Water-soluble eumelanin as a PCR-inhibitor and a simple method for its removal. *Nihon Hoigaku Zasshi= Jpn. J. Leg. Med.* **47**, 323–329 (1993).
12. Katcher, H. & Schwartz, I. A distinctive property of Tth DNA polymerase: enzymatic amplification in the presence of phenol. *Biotechniques* **16**, 84–92 (1994).
13. Tsai, Y.-L. & Olson, B. Rapid method for separation of bacterial DNA from humic substances in sediments for polymerase chain reaction. *Appl. Environ. Microbiol.* **58**, 2292–2295 (1992).
14. Bélec, L. et al. Myoglobin as a polymerase chain reaction (PCR) inhibitor: a limitation for PCR from skeletal muscle tissue avoided by the use of thermus thermophilus polymerase. *Muscle Nerve* **21**, 1064–1067 (1998).
15. Kim, C.-H. et al. Optimization of the PCR for detection of Staphylococcus aureus nuc gene in bovine milk. *J. Dairy Sci.* **84**, 74–83 (2001).
16. Bickley, J., Short, J., McDowell, D. & Parkes, H. Polymerase chain reaction (PCR) detection of Listeria monocytogenes in diluted milk and reversal of PCR inhibition caused by calcium ions. *Lett. Appl. Microbiol.* **22**, 153–158 (1996).
17. Monteiro, L. et al. Complex polysaccharides as PCR inhibitors in feces: Helicobacter pylori model. *J. Clin. Microbiol.* **35**, 995–998 (1997).
18. Demeke, T. & Adams, R. P. The effects of plant polysaccharides and buffer additives on PCR. *Biotechniques* **12**, 332–334 (1992).
19. Khan, G., Kangro, H., Coates, P. & Heath, R. Inhibitory effects of urine on the polymerase chain reaction for cytomegalovirus DNA. *J. Clin. Pathol.* **44**, 360–365 (1991).
20. Yuce, M., Kurt, H., Mokkapati, V. R. & Budak, H. Employment of nanomaterials in polymerase chain reaction: insight into the impacts and putative operating mechanisms of nano- additives in PCR. *RSC Adv.* **4**, 36800–36814 (2014).
21. Khan, I., Saeed, K. & Khan, I. Nanoparticles: Properties, applications and toxicities. *Arab. J. Chem.* **12**, 908–931 (2019).
22. Yang, W., Li, X., Sun, J. & Shao, Z. Enhanced PCR amplification of GC-rich DNA templates by gold nanoparticles. *ACS Appl. Mater. interfaces* **5**, 11520–11524 (2013).
23. Rehman, A. et al. Metal nanoparticle assisted polymerase chain reaction for strain typing of Salmonella typhi. *Analyst* **140**, 7366–7372 (2015).
24. Cui, D., Tian, F., Kong, Y., Titushikin, I. & Gao, H. Effects of single-walled carbon nanotubes on the polymerase chain reaction. *Nanotechnology* **15**, 154 (2003).
25. Zhang, Z., Wang, M. & An, H. An aqueous suspension of carbon nanopowder enhances the efficiency of a polymerase chain reaction. *Nanotechnology* **18**, 355706 (2007).
26. Madadelahi, M., Ghazimirsaeed, E. & Shamloo, A. Design and fabrication of a two-phase diamond nanoparticle aided fast PCR device. *Analytica Chim. Acta* **1068**, 28–40 (2019).
27. Jia, J., Sun, L., Hu, N., Huang, G. & Weng, J. Graphene enhances the specificity of the polymerase chain reaction. *Small* **8**, 2011–2015 (2012).
28. Nie, L., Gao, L., Yan, X. & Wang, T. Functionalized tetrapod-like ZnO nanostructures for plasmid DNA purification, polymerase chain reaction and delivery. *Nanotechnology* **18**, 015101 (2006).
29. Li, S. et al. Impact and mechanism of TiO_2 nanoparticles on DNA synthesis in vitro. *Sci. China Ser. B: Chem.* **51**, 367–372 (2008).
30. Wang, Y., Wang, F., Wang, H. & Song, M. Graphene oxide enhances the specificity of the polymerase chain reaction by modifying primer-template matching. *Sci. Rep.* **7**, 16510 (2017).
31. Wang, L. et al. Effects of quantum dots in polymerase chain reaction. *J. Phys. Chem. B* **113**, 7637–7641 (2009).
32. Almond, D. P. & Patel, P. *Photothermal Science and Techniques* (Springer Science & Business Media, 1996).
33. Cui, X. et al. Photothermal nanomaterials: a powerful light-to-heat converter. *Chem. Rev.* **123**, 6891–6952 (2023).
34. Jauffred, L., Samadi, A., Klingberg, H., Bendix, P. M. & Oddershede, L. B. Plasmonic heating of nanostructures. *Chem. Rev.* **119**, 8087–8130 (2019).
35. Kim, M., Lee, J.-H. & Nam, J.-M. Plasmonic photothermal nanoparticles for biomedical applications. *Adv. Sci.* **6**, 1900471 (2019).
36. Huang, X. et al. Design and functionalization of the NIR-responsive photothermal semiconductor nanomaterials for cancer theranostics. *Acc. Chem. Res.* **50**, 2529–2538 (2017).
37. Kriegel, I., Scotognella, F. & Manna, L. Plasmonic doped semiconductor nanocrystals: properties, fabrication, applications and perspectives. *Phys. Rep.* **674**, 1–52 (2017).
38. Panwar, N. et al. Nanocarbons for biology and medicine: sensing, imaging, and drug delivery. *Chem. Rev.* **119**, 9559–9656 (2019).
39. Hong, G., Diao, S., Antaris, A. L. & Dai, H. Carbon nanomaterials for biological imaging and nanomedicinal therapy. *Chem. Rev.* **115**, 10816–10906 (2015).
40. Wang, B. et al. Carbon dots as a new class of nanomedicines: opportunities and challenges. *Coord. Chem. Rev.* **442**, 214010 (2021).
41. Du, J., Xu, N., Fan, J., Sun, W. & Peng, X. Carbon dots for in vivo bioimaging and theranostics. *Small* **15**, 1805087 (2019).
42. Jung, H. S. et al. Organic molecule-based photothermal agents: an expanding photothermal therapy universe. *Chem. Soc. Rev.* **47**, 2280–2297 (2018).
43. Zhao, L., Liu, Y., Xing, R. & Yan, X. Supramolecular photothermal effects: a promising mechanism for efficient thermal conversion. *Angew. Chem.* **132**, 3821–3829 (2020).
44. Cai, G., Yan, P., Zhang, L., Zhou, H.-C. & Jiang, H.-L. Metal–organic framework-based hierarchically porous materials: synthesis and applications. *Chem. Rev.* **121**, 12278–12326 (2021).
45. Chakraborty, G., Park, I.-H., Medishetty, R. & Vittal, J. J. Two-dimensional metal-organic framework materials: synthesis, structures, properties and applications. *Chem. Rev.* **121**, 3751–3891 (2021).
46. Wang, Q. & Astruc, D. State of the art and prospects in metal–organic framework (MOF)- based and MOF-derived nanocatalysis. *Chem. Rev.* **120**, 1438–1511 (2019).
47. Xiao, J.-D. & Jiang, H.-L. Metal–organic frameworks for photocatalysis and photothermal catalysis. *Acc. Chem. Res.* **52**, 356–366 (2018).
48. Lan, G., Ni, K. & Lin, W. Nanoscale metal–organic frameworks for phototherapy of cancer. *Coord. Chem. Rev.* **379**, 65–81 (2019).
49. VahidMohammadi, A., Rosen, J. & Gogotsi, Y. The world of two-dimensional carbides and nitrides (MXenes). *Science* **372**, eabf1581 (2021).
50. Hantanasirisakul, K. & Gogotsi, Y. Electronic and optical properties of 2D transition metal carbides and nitrides (MXenes). *Adv. Mater.* **30**, 1804779 (2018).
51. Szuplewska, A. et al. Future applications of MXenes in biotechnology, nanomedicine, and sensors. *Trends Biotechnol.* **38**, 264–279 (2020).
52. Mi, Z. et al. Stable radical cation-containing covalent organic frameworks exhibiting remarkable structure-enhanced photothermal conversion. *J. Am. Chem. Soc.* **141**, 14433–14442 (2019).
53. Ma, H.-C., Zhao, C.-C., Chen, G.-J. & Dong, Y.-B. Photothermal conversion triggered thermal asymmetric catalysis within metal nanoparticles loaded homochiral covalent organic framework. *Nat. Commun.* **10**, 3368 (2019).
54. Xia, R. et al. Nanoscale covalent organic frameworks with donor–acceptor structure for enhanced photothermal ablation of tumors. *ACS Nano* **15**, 7638–7648 (2021).
55. Tan, J. et al. Manipulation of amorphous-to-crystalline transformation: Towards the construction of covalent organic framework hybrid microspheres with NIR photothermal conversion ability. *Angew. Chem. Int. Ed.* **55**, 13979–13984 (2016).
56. Agrawal, A. et al. Localized surface plasmon resonance in semiconductor nanocrystals. *Chem. Rev.* **118**, 3121–3207 (2018).
57. Georgakilas, V., Perman, J. A., Tucek, J. & Zboril, R. Broad family of carbon nanoallotropes: classification, chemistry, and applications of fullerenes,

carbon dots, nanotubes, graphene, nanodiamonds, and combined superstructures. *Chem. Rev.* **115**, 4744–4822 (2015).
58. Li, Z., Lei, H., Kan, A., Xie, H. & Yu, W. Photothermal applications based on graphene and its derivatives: a state-of-the-art review. *Energy* **216**, 119262 (2021).
59. Zhao, L., Liu, Y., Chang, R., Xing, R. & Yan, X. Supramolecular photothermal nanomaterials as an emerging paradigm toward precision cancer therapy. *Adv. Funct. Mater.* **29**, 1806877 (2019).
60. Kim, H. J., Kim, B., Auh, Y. & Kim, E. Conjugated organic photothermal films for spatiotemporal thermal engineering. *Adv. Mater.* **33**, 2005940 (2021).
61. He, W. et al. Structure development of carbon-based solar-driven water evaporation systems. *Sci. Bull.* **66**, 1472–1483 (2021).
62. Yang, S.-M., Lv, S., Zhang, W. & Cui, Y. Microfluidic point-of-care (POC) devices in early diagnosis: a review of opportunities and challenges. *Sensors* **22**, 1620 (2022).
63. Liu, H., Dao, T. N. T., Koo, B., Jang, Y. O. & Shin, Y. Trends and challenges of nanotechnology in self-test at home. *TrAC Trends Anal. Chem.* **144**, 116438 (2021).
64. Bartosik, M. et al. Advanced technologies towards improved HPV diagnostics. *J. Med. Virol.* **96**, e29409 (2024).
65. Xin, H., Namgung, B. & Lee, L. P. Nanoplasmonic optical antennas for life sciences and medicine. *Nat. Rev. Mater.* **3**, 228–243 (2018).
66. Rådström, P., Löfström, C., Lövenklev, M., Knutsson, R. & Wolffs, P. Strategies for overcoming PCR inhibition. *Cold Spring Harb. Protoc.* **2008**, pdb–top20 (2008).
67. Yang, Z. et al. Application of nanomaterials to enhance polymerase chain reaction. *Molecules* **27**, 8854 (2022).
68. Lou, X. & Zhang, Y. Mechanism studies on nanoPCR and applications of gold nanoparticles in genetic analysis. *ACS Appl. Mater. interfaces* **5**, 6276–6284 (2013).
69. Li, M., Lin, Y.-C., Wu, C.-C. & Liu, H.-S. Enhancing the efficiency of a PCR using gold nanoparticles. *Nucleic Acids Res.* **33**, e184–e184 (2005).
70. Yuan, L. & He, Y. Effect of surface charge of PDDA-protected gold nanoparticles on the specificity and efficiency of DNA polymerase chain reaction. *Analyst* **138**, 539–545 (2013).
71. Li, A. et al. Mechanistic studies of enhanced PCR using PEGylated PEI-entrapped gold nanoparticles. *ACS Appl. Mater. Interfaces* **8**, 25808–25817 (2016).
72. Jeong, H. Y. et al. A hybrid composite of gold and graphene oxide as a PCR enhancer. *RSC Adv.* **5**, 93117–93121 (2015).
73. Fu-Ming, S., Xin, L. & Jia, L. Development of nano-polymerase chain reaction and its application. *Chin. J. Anal. Chem.* **45**, 1745–1753 (2017).
74. Ye, J. et al. Development of a triple NanoPCR method for feline calicivirus, feline panleukopenia syndrome virus, and feline herpesvirus type I virus. *BMC Vet. Res.* **18**, 379 (2022).
75. Vanzha, E. et al. Gold nanoparticle-assisted polymerase chain reaction: effects of surface ligands, nanoparticle shape and material. *RSC Adv.* **6**, 110146–110154 (2016).
76. Uysal, E. Impacts of Single-walled Carbon Nanotubes on Polymerase Chain Reaction. PhD thesis, Technological University Dublin (2015).
77. Liu, P., Guan, R., Liu, M. & Huang, G. et al. Effect of PCR amplification with nano-silver on DNA synthesis and its mechanism. *J. Agric. Biotechnol.* **18**, 876–881 (2010).
78. Hwang, S.-H. et al. Effects of upconversion nanoparticles on polymerase chain reaction. *PLoS ONE* **8**, e73408 (2013).
79. Hu, C. et al. Graphene oxide-based qRT-PCR assay enables the sensitive and specific detection of miRNAs for the screening of ovarian cancer. *Analytica Chim. Acta* **1174**, 338715 (2021).
80. Lenka, G. & Weng, W.-H. Nanosized particles of titanium dioxide specifically increase the efficency of conventional polymerase chain reaction. *Digest J. Nanomater. Biostruct. (DJNB)* **8** (2013).
81. Shen, C. et al. NanoPCR observation: different levels of DNA replication fidelity in nanoparticle-enhanced polymerase chain reactions. *Nanotechnology* **20**, 455103 (2009).
82. Willets, K. A. & Van Duyne, R. P. Localized surface plasmon resonance spectroscopy and sensing. *Annu. Rev. Phys. Chem.* **58**, 267–297 (2007).
83. Mayer, K. M. & Hafner, J. H. Localized surface plasmon resonance sensors. *Chem. Rev.* **111**, 3828–3857 (2011).
84. Zheng, J. et al. Gold nanorods: the most versatile plasmonic nanoparticles. *Chem. Rev.* **121**, 13342–13453 (2021).
85. Ha, M. et al. Multicomponent plasmonic nanoparticles: from heterostructured nanoparticles to colloidal composite nanostructures. *Chem. Rev.* **119**, 12208–12278 (2019).
86. Deng, Z. et al. The emergence of solar thermal utilization: solar-driven steam generation. *J. Mater. Chem. A* **5**, 7691–7709 (2017).
87. Stoneham, A. Non-radiative transitions in semiconductors. *Rep. Prog. Phys.* **44**, 1251 (1981).
88. Liu, X. et al. Noble metal–metal oxide nanohybrids with tailored nanostructures for efficient solar energy conversion, photocatalysis and environmental remediation. *Energy Environ. Sci.* **10**, 402–434 (2017).
89. Coughlan, C. et al. Compound copper chalcogenide nanocrystals. *Chem. Rev.* **117**, 5865–6109 (2017).
90. Woods-Robinson, R. et al. Wide band gap chalcogenide semiconductors. *Chem. Rev.* **120**, 4007–4055 (2020).
91. Chen, X., Liu, L., Yu, P. Y. & Mao, S. S. Increasing solar absorption for photocatalysis with black hydrogenated titanium dioxide nanocrystals. *Science* **331**, 746–750 (2011).
92. Wang, J. et al. High-performance photothermal conversion of narrow-bandgap Ti_2O_3 nanoparticles. *Adv. Mater.* **29**, 1603730 (2017).
93. Shockley, W. & Read, W. Jr. Statistics of the recombinations of holes and electrons. *Phys. Rev.* **87**, 835 (1952).
94. Ghoussoub, M., Xia, M., Duchesne, P. N., Segal, D. & Ozin, G. Principles of photothermal gas-phase heterogeneous CO_2 catalysis. *Energy Environ. Sci.* **12**, 1122–1142 (2019).
95. Zhu, L., Gao, M., Peh, C. K. N. & Ho, G. W. Solar-driven photothermal nanostructured materials designs and prerequisites for evaporation and catalysis applications. *Mater. Horiz.* **5**, 323–343 (2018).
96. Cheng, P., Wang, D. & Schaaf, P. A review on photothermal conversion of solar energy with nanomaterials and nanostructures: from fundamentals to applications. *Adv. Sustain. Syst.* **6**, 2200115 (2022).
97. Ye, E. & Li, Z. *Photothermal Nanomaterials* (Royal Society of Chemistry, 2022).
98. Cunha, J. et al. Controlling light, heat, and vibrations in plasmonics and phononics. *Adv. Opt. Mater.* **8**, 2001225 (2020).
99. Baffou, G. in *Thermoplasmonics: Heating Metal Nanoparticles Using Light* 36–80 (Cambridge University Press, 2017).
100. Zeng, J., Goldfeld, D. & Xia, Y. A plasmon-assisted optofluidic system for measuring the photothermal conversion efficiencies of gold nanostructures and controlling an electrical switch. *Angew. Chem. (Int. ed. Engl.)* **52**, 4169 (2013).
101. Xiao, L., Chen, X., Yang, X., Sun, J. & Geng, J. Recent advances in polymer-based photothermal materials for biological applications. *ACS Appl. Polym. Mater.* **2**, 4273–4288 (2020).
102. Paściak, A., Pilch-Wróbel, A., Marciniak, Ł., Schuck, P. J. & Bednarkiewicz, A. Standardization of methodology of light-to-heat conversion efficiency determination for colloidal nanoheaters. *ACS Appl. Mater. Interfaces* **13**, 44556–44567 (2021).
103. Roper, D. K., Ahn, W. & Hoepfner, M. Microscale heat transfer transduced by surface plasmon resonant gold nanoparticles. *J. Phys. Chem. C.* **111**, 3636–3641 (2007).
104. Chen, J., Ye, Z., Yang, F. & Yin, Y. Plasmonic nanostructures for photothermal conversion. *Small Sci.* **1**, 2000055 (2021).
105. Gusain, R., Kumar, N. & Ray, S. S. Recent advances in carbon nanomaterial-based adsorbents for water purification. *Coord. Chem. Rev.* **405**, 213111 (2020).
106. Wang, Y., Meng, H.-M., Song, G., Li, Z. & Zhang, X.-B. Conjugated-polymer-based nanomaterials for photothermal therapy. *ACS Appl. Polym. Mater.* **2**, 4258–4272 (2020).
107. Xie, Z. et al. The rise of 2D photothermal materials beyond graphene for clean water production. *Adv. Sci.* **7**, 1902236 (2020).
108. Ahrberg, C. D. et al. Plasmonic heating-based portable digital PCR system. *Lab Chip* **20**, 3560–3568 (2020).
109. Nabuti, J., Elbab, A. R. F., Abdel-Mawgood, A., Yoshihisa, M. & Shalaby, H. M. Highly efficient photonic PCR system based on plasmonic heating of gold nanofilms. *Biosens. Bioelectron. X* **14**, 100346 (2023).
110. Son, J. H. et al. Ultrafast photonic PCR. *Light Sci. Appl.* **4**, e280–e280 (2015).
111. AbdElFatah, T. et al. Nanoplasmonic amplification in microfluidics enables accelerated colorimetric quantification of nucleic acid biomarkers from pathogens. *Nat. Nanotechnol.* **18**, 922–932 (2023).
112. Monshat, H., Wu, Z., Pang, J., Zhang, Q. & Lu, M. Integration of plasmonic heating and on-chip temperature sensor for nucleic acid amplification assays. *J. Biophotonics* **13**, e202000060 (2020).

113. Lim, S. et al. Transparent and stretchable capacitive pressure sensor using selective plasmonic heating-based patterning of silver nanowires. *Appl. Surf. Sci.* **561**, 149989 (2021).
114. Wang, P. et al. 3D plasmonic nanostructure-based polarized ECL sensor for exosome detection in tumor microenvironment. *ACS Sens.* **8**, 1782–1791 (2023).
115. Pyrak, E., Kowalczyk, A., Weyher, J. L., Nowicka, A. M. & Kudelski, A. Influence of sandwich- type DNA construction strategy and plasmonic metal on signal generated by SERS DNA sensors. *Spectrochim. Acta A: Mol. Biomol. Spectrosc.* **295**, 122606 (2023).
116. Moreira, P. et al. Plasmonic genosensor for detecting hazelnut Cor a 14-encoding gene for food allergen monitoring. *Analytica Chim. Acta* **1259**, 341168 (2023).
117. Rizalputri, L. N. et al. Preliminary study for the development of a solution phase localized surface plasmon resonance (LSPR) biosensor based on gold nanoparticle to detect SARS-CoV- 2. *AIP Conf. Proc.* **2580** (2023).
118. Qiu, G. et al. Dual-functional plasmonic photothermal biosensors for highly accurate severe acute respiratory syndrome coronavirus 2 detection. *ACS Nano* **14**, 5268–5277 (2020).
119. Spitzberg, J. D., Zrehen, A., van Kooten, X. F. & Meller, A. Plasmonic-nanopore biosensors for superior single-molecule detection. *Adv. Mater.* **31**, 1900422 (2019).
120. Ishii, S., Sugavaneshwar, R. P. & Nagao, T. Titanium nitride nanoparticles as plasmonic solar heat transducers. *J. Phys. Chem. C* **120**, 2343–2348 (2016).
121. Borghei, Y.-S., Hosseinkhani, S. & Ganjali, M. R. "Plasmonic Nanomaterials": an emerging avenue in biomedical and biomedical engineering opportunities. *J. Adv. Res.* **39**, 61–71 (2022).
122. Monshat, H. Application of Plasmonic Devices in Spectroscopy and Biomedical Studies. PhD thesis, Iowa State University (2020).
123. De la Encarnación, C., de Aberasturi, D. J. & Liz-Marzán, L. M. Multifunctional plasmonic- magnetic nanoparticles for bioimaging and hyperthermia. *Adv. Drug Deliv. Rev.* **189**, 114484 (2022).
124. Lee, S., Sun, Y., Cao, Y. & Kang, S. H. Plasmonic nanostructure-based bioimaging and detection techniques at the single-cell level. *TrAC Trends Anal. Chem.* **117**, 58–68 (2019).
125. Donner, J. S. et al. Imaging of plasmonic heating in a living organism. *Acs Nano* **7**, 8666–8672 (2013).
126. Psarski, M., Lech, A. & Celichowski, G. Plasmonic heating of protected silver nanowires for anti-frosting superhydrophobic coating. *Nanotechnology* **33**, 465205 (2022).
127. Zhong, H. et al. Plasmonic and superhydrophobic self-decontaminating N95 respirators. *ACS nano* **14**, 8846–8854 (2020).
128. Qiu, Y. et al. Ultrasensitive plasmonic photothermal immunomagnetic bioassay using real- time and end-point dual-readout. *Sens. Actuators B: Chem.* **377**, 133110 (2023).
129. Quintanilla, M. et al. Thermal monitoring during photothermia: hybrid probes for simultaneous plasmonic heating and near-infrared optical nanothermometry. *Theranostics* **9**, 7298 (2019).
130. Zhang, W. et al. Atomic switches of metallic point contacts by plasmonic heating. *Light Sci. Appl.* **8**, 34 (2019).
131. Wang, L. et al. Laser-induced plasmonic heating on silver nanoparticles/poly (N-isopropylacrylamide) mats for optimizing SERS detection. *J. Raman Spectrosc.* **48**, 243–250 (2017).
132. Enders, M., Mukai, S., Uwada, T. & Hashimoto, S. Plasmonic nanofabrication through optical heating. *J. Phys. Chem. C* **120**, 6723–6732 (2016).
133. Fedoruk, M., Meixner, M., Carretero-Palacios, S., Lohmüller, T. & Feldmann, J. Nanolithography by plasmonic heating and optical manipulation of gold nanoparticles. *ACS Nano* **7**, 7648–7653 (2013).
134. Chiu, C.-S., Chen, H.-Y., Hsiao, C.-F., Lin, M.-H. & Gwo, S. Ultrasensitive surface acoustic wave detection of collective plasmonic heating by close-packed colloidal gold nanoparticles arrays. *J. Phys. Chem. C* **117**, 2442–2448 (2013).
135. Xu, Z., Rao, N., Tang, C.-Y. & Law, W.-C. Seawater desalination by interfacial solar vapor generation method using plasmonic heating nanocomposites. *Micromachines* **11**, 867 (2020).
136. Zhang, L. et al. Plasmonic heating from indium nanoparticles on a floating microporous membrane for enhanced solar seawater desalination. *Nanoscale* **9**, 12843–12849 (2017).
137. Warkentin, C. L., Yu, Z., Sarkar, A. & Frontiera, R. R. Decoding chemical and physical processes driving plasmonic photocatalysis using surface-enhanced Raman spectroscopies. *Acc. Chem. Res.* **54**, 2457–2466 (2021).
138. Sarhan, R. M. et al. The importance of plasmonic heating for the plasmon-driven photodimerization of 4-nitrothiophenol. *Sci. Rep.* **9**, 3060 (2019).
139. Li, F. et al. Plasmonic local heating induced strain modulation for enhanced efficiency and stability of perovskite solar cells. Advanced Energy. *Materials* **12**, 2200186 (2022).
140. Auer, S. K. Rapid Plasmonic Actuation of Thermoresponsive Hydrogel Structures. PhD thesis, Vienna University of Technology (2022).
141. Ringe, E. et al. Plasmon length: a universal parameter to describe size effects in gold nanoparticles. *J. Phys. Chem. Lett.* **3**, 1479–1483 (2012).
142. Ringe, E. et al. Correlating the structure and localized surface plasmon resonance of single silver right bipyramids. *Nanotechnology* **23**, 444005 (2012).
143. Zhu, J. et al. Additive controlled synthesis of gold nanorods (GNRs) for two-photon luminescence imaging of cancer cells. *Nanotechnology* **21**, 285106 (2010).
144. Ye, X. et al. Seeded growth of monodisperse gold nanorods using bromide-free surfactant mixtures. *Nano Lett.* **13**, 2163–2171 (2013).
145. Xi, Z. et al. Improving lyophilization and long-term stability of gold nanostars for photothermal applications. *ACS Appl. Nano Mater.* **6**, 17336–17346 (2023).
146. Guo, Z. et al. Intrinsic optical properties and emerging applications of gold nanostructures. *Adv. Mater.* **35**, 2206700 (2023).
147. Zhang, H., Zhu, T. & Li, M. Quantitative analysis of the shape effect of thermoplasmonics in gold nanostructures. *J. Phys. Chem. Lett.* **14**, 3853–3860 (2023).
148. Lindley, S. A. & Zhang, J. Z. Bumpy hollow gold nanospheres for theranostic applications: effect of surface morphology on photothermal conversion efficiency. *ACS Appl. Nano Mater.* **2**, 1072–1081 (2019).
149. Yin, B. et al. A multilayered mesoporous gold nanoarchitecture for ultra-effective near-infrared light-controlled chemo/photothermal therapy for cancer guided by SERS imaging. *Small* **19**, 2206762 (2023).
150. Zhou, G. et al. Renal clearable catalytic 2d au–porphyrin coordination polymer augmented photothermal-gas synergistic cancer therapy. *Small* **19**, 2206749 (2023).
151. Zhang, S. et al. An NIR-II photothermally triggered "oxygen bomb" for hypoxic tumor programmed cascade therapy. *Adv. Mater.* **34**, 2201978 (2022).
152. Liu, Y. et al. Photothermal conversion of gold nanoparticles for uniform pulsed laser warming of vitrified biomaterials. *Nanoscale* **12**, 12346–12356 (2020).
153. Liu, W. et al. Black silver nanocubes@ amino acid-encoded highly branched gold shells with efficient photothermal conversion for tumor therapy. *ACS Appl. Mater. Interfaces* **15**, 236–248 (2022).
154. Lv, Z., He, S., Wang, Y. & Zhu, X. Noble metal nanomaterials for NIR-triggered photothermal therapy in cancer. *Adv. Healthc. Mater.* **10**, 2001806 (2021).
155. Sun, Y. et al. Porous biomass foam of polypyrrole-coated cattail fibers for efficient photothermal evaporation. *Ind. Crops Products* **178**, 114559 (2022).
156. Webb, J. A. & Bardhan, R. Emerging advances in nanomedicine with engineered gold nanostructures. *Nanoscale* **6**, 2502–2530 (2014).
157. Pant, A., Davis, E. J. & Pauzauskie, P. J. Photothermal heating of semiconductor nanoribbons. *J. Phys. Chem. C* **123**, 28941–28947 (2019).
158. Chen, Z. et al. Morphology-controlled synthesis of Cu_2O encapsulated phase change materials: Photothermal conversion and storage performance in visible light regime. *Chem. Eng. J.* **454**, 140089 (2023).
159. Li, R., Zhang, L., Shi, L. & Wang, P. MXene Ti_3C_2: an effective 2D light-to-heat conversion material. *ACS Nano* **11**, 3752–3759 (2017).
160. Tarasenka, N. et al. Laser synthesis and optical properties of hybrid silicon nanostructures for photothermal conversion of solar radiation. *J. Appl. Spectrosc.* **90**, 346–357 (2023).
161. Kim, J., Kim, H., Park, J. H. & Jon, S. Gold nanorod-based photo-PCR system for one-step, rapid detection of bacteria. *Nanotheranostics* **1**, 178 (2017).
162. Roche, P. J. et al. Real time plasmonic qPCR: how fast is ultra-fast? 30 cycles in 54 seconds. *Analyst* **142**, 1746–1755 (2017).
163. Aizudin, M. et al. Sustainable development of graphitic carbon nanosheets from plastic wastes with efficient photothermal energy conversion for enhanced solar evaporation. *J. Mater. Chem. A* **10**, 19612–19617 (2022).
164. Zhou, Q. et al. A graphene assembled porous fiber-based Janus membrane for highly effective solar steam generation. *J. Colloid Interface Sci.* **592**, 77–86 (2021).
165. Zhu, J. et al. Carbon materials for enhanced photothermal conversion: preparation and applications on steam generation. *Mater. Rep. Energy* **4**, 100245 (2023).

166. Chen, G. et al. Structural and compositional modulation of porous carbon for high-performance photothermal water evaporation. *ACS Sustain. Chem. Eng.* **10**, 4013–4021 (2022).
167. Yu, Y. et al. Ultra-black and self-cleaning all carbon nanotube hybrid films for efficient water desalination and purification. *Carbon* **169**, 134–141 (2020).
168. Kock, W. E. Metallic delay lenses. *Bell Syst. Tech. J.* **27**, 58–82 (1948).
169. Howes, K. & Whitehead, E. The refractive index of a dielectric loaded with thin metal strips. Report from the Research Laboratories of Elliott Brothers (London) Ltd., Boreham Wood (Herts.) (1949).
170. Brown, J. The design of metallic delay dielectrics. *Proc. IEE—Part III: Radio Commun. Eng.* **97**, 45–48 (1950).
171. Veselago, V. The electrodynamics of substances with simultaneously negative values of and. *Usp. Fiz. Nauk* **92**, 517–526 (1967).
172. Smith, D. R., Padilla, W. J., Vier, D., Nemat-Nasser, S. C. & Schultz, S. Composite medium with simultaneously negative permeability and permittivity. *Phys. Rev. Lett.* **84**, 4184 (2000).
173. Kadic, M., Milton, G. W., van Hecke, M. & Wegener, M. 3D metamaterials. *Nat. Rev. Phys.* **1**, 198–210 (2019).
174. Holliman, J. E., Schaef, H. T., McGrail, B. P. & Miller, Q. R. Review of foundational concepts and emerging directions in metamaterial research: design, phenomena, and applications. *Mater. Adv.* **3**, 8390–8406 (2022).
175. Zhao, D. et al. Recent advances in ultraviolet nanophotonics: from plasmonics and metamaterials to metasurfaces. *Nanophotonics* **10**, 2283–2308 (2021).
176. Ji, W. et al. Recent advances in metasurface design and quantum optics applications with machine learning, physics-informed neural networks, and topology optimization methods. *Light Sci. Appl.* **12**, 169 (2023).
177. Park, E. et al. 3-D/4-D-printed reconfigurable metasurfaces for controlling electromagnetic waves. *Proc. IEEE* (2024).
178. Lee, Y. Y., Kim, R. M., Im, S. W., Balamurugan, M. & Nam, K. T. Plasmonic metamaterials for chiral sensing applications. *Nanoscale* **12**, 58–66 (2020).
179. Wang, P. et al. Molecular plasmonics with metamaterials. *Chem. Rev.* **122**, 15031–15081 (2022).
180. Wang, P. et al. Plasmonic metamaterials for nanochemistry and sensing. *Acc. Chem. Res.* **52**, 3018–3028 (2019).
181. Chakravarty, U., Khare, J., Joshi, M., Mukherjee, C. & Singh, R. Broad band optical absorption and thermoplasmonic response from bio-inspired hierarchical copper nanostructures fabricated by pulsed laser deposition. *Opt. Laser Technol.* **167**, 109772 (2023).
182. Rogez, B., Marmri, Z., Thibaudau, F. & Baffou, G. Thermoplasmonics of metal layers and nanoholes. *APL Photonics* **6** (2021).
183. Shin, D. et al. Photothermal metamaterials for solar energy applications. *Adv. Opt. Mater.* **6**, 10–1002 (2018).
184. Zhao, Y. et al. Hyperbolic metamaterial nanoparticles random array for thermoplasmonics in the II and III near-infrared windows. *Appl. Phys. Lett.* **122** (2023).
185. Petronella, F. et al. Thermoplasmonic controlled optical absorber based on a liquid crystal metasurface. *ACS Appl. Mater. Interfaces* **15**, 49468–49477 (2023).
186. Zaheri-Ghannad, S., Kordzadeh-Kermani, V. & Madadelahi, M. Acoustic-assisted centrifugal microfluidics for particle/cell separation. *Chem. Eng. Process.-Process Intensif.* **201**, 109803 (2024).
187. Rahdar, M., Madadelahi, M. & Namazi, M. Microfiber generation on centrifugal microfluidic platforms using fluidic barriers. *Chem. Eng. Process.-Process Intensif.* **193**, 109553 (2023).
188. Kordzadeh-Kermani, V. et al. Electrified lab on disc systems: a comprehensive review on electrokinetic applications. *Biosens. Bioelectron.* **214**, 114381 (2022).
189. Madadelahi, M., Acosta-Soto, L. F., Hosseini, S., Martinez-Chapa, S. O. & Madou, M. J. Mathematical modeling and computational analysis of centrifugal microfluidic platforms: a review. *Lab Chip* **20**, 1318–1357 (2020).
190. Kordzadeh-Kermani, V., Ashrafizadeh, S. N. & Madadelahi, M. Dielectrophoretic separation/classification/focusing of microparticles using electrified lab-on-a-disc platforms. *Analytica Chim. Acta* **1310**, 342719 (2024).
191. Kordzadeh-Kermani, V., Dartoomi, H., Azizi, M., Ashrafizadeh, S. N. & Madadelahi, M. Investigating the performance of the multi-lobed leaf-shaped oscillatory obstacles in micromixers using bulk acoustic waves (BAW): mixing and chemical reaction. *Micromachines* **14**, 795 (2023).
192. Madadelahi, M., Azimi-Boulali, J., Madou, M. & Martinez-Chapa, S. O. Characterization of fluidic-barrier-based particle generation in centrifugal microfluidics. *Micromachines* **13**, 881 (2022).
193. Azimi-Boulali, J., Madadelahi, M., Madou, M. J. & Martinez-Chapa, S. O. Droplet and particle generation on centrifugal microfluidic platforms: A review. *Micromachines* **11**, 603 (2020).
194. Sengupta, P., Khanra, K., Chowdhury, A. R. & Datta, P. In: Pal, K. et al. (eds) *Bioelectronics and Medical Devices* 47–95 (Elsevier, 2019).
195. Mejia-Salazar, J. R., Rodrigues Cruz, K., Materon Vasques, E. M. & Novais de Oliveira Jr, O. Microfluidic point-of-care devices: New trends and future prospects for ehealth diagnostics. *Sensors* **20**, 1951 (2020).
196. Hwu, A. T. et al. Centrifugal disc liquid reciprocation flow considerations for antibody binding to COVID antigen array during microfluidic integration. *Lab a Chip* **22**, 2695–2706 (2022).
197. Son, J. H. et al. Rapid optical cavity PCR. Advanced Healthcare. *Materials* **5**, 167–174 (2016).
198. Cho, B. et al. Nanophotonic cell lysis and polymerase chain reaction with gravity-driven cell enrichment for rapid detection of pathogens. *ACS nano* **13**, 13866–13874 (2019).
199. Lee, B., Lee, Y., Kim, S.-M., Kim, K. & Kim, M.-G. Rapid membrane-based photothermal PCR for disease detection. *Sens. Actuators B: Chem.* **360**, 131554 (2022).
200. Amadeh, A., Ghazimirsaeed, E., Shamloo, A. & Dizani, M. Improving the performance of a photonic PCR system using TiO_2 nanoparticles. *J. Ind. Eng. Chem.* **94**, 195–204 (2021).
201. Lee, Y. et al. Nanoplasmonic on-chip PCR for rapid precision molecular diagnostics. *ACS Appl. Mater. interfaces* **12**, 12533–12540 (2020).
202. Kang, B.-H. et al. Ultrafast and real-time nanoplasmonic on-chip polymerase chain reaction for rapid and quantitative molecular diagnostics. *ACS nano* **15**, 10194–10202 (2021).
203. Kang, B.-H. et al. Ultrafast Plasmonic Nucleic Acid Amplification and Real-Time Quantification for Decentralized Molecular Diagnostics. *ACS nano* **17**, 6507–6518 (2023).
204. Chae, W. R., Song, Y.-J. & Lee, N. Y. Polydopamine-mediated gold nanoparticle coating strategy and its application in photothermal polymerase chain reaction. Lab Chip **25**, 1429–1438 (2024).
205. Li, H. et al. Nanoparticle PCR: nanogold-assisted PCR with enhanced specificity. *Angew. Chem. Int. Ed.* **44**, 5100–5103 (2005).
206. Pan, J. et al. Nanogold-assisted multi-round polymerase chain reaction (PCR). *J. Nanosci. Nanotechnol.* **7**, 4428–4433 (2007).
207. Mi, L., Zhu, H., Zhang, X., Hu, J. & Fan, C. Mechanism of the interaction between Au nanoparticles and polymerase in nanoparticle PCR. *Chin. Sci. Bull.* **52**, 2345–2349 (2007).
208. Lin, Y. et al. Mechanism of gold nanoparticle induced simultaneously increased PCR efficiency and specificity. *Chin. Sci. Bull.* **58**, 4593–4601 (2013).
209. Mandal, S., Hossain, M., Muruganandan, T., Kumar, G. S. & Chaudhuri, K. Gold nanoparticles alter Taq DNA polymerase activity during polymerase chain reaction. *RSC Adv.* **3**, 20793–20799 (2013).
210. Chen, J. et al. A highly effective polymerase chain reaction enhancer based on dendrimer-entrapped gold nanoparticles. *Analyst* **137**, 223–228 (2012).
211. Zhang, Z., Shen, C., Wang, M., Han, H. & Cao, X. Aqueous suspension of carbon nanotubes enhances the specificity of long PCR. *Biotechniques* **44**, 537–545 (2008).
212. Cao, X. et al. Effect of surface charge of polyethyleneimine-modified multi-walled carbon nanotubes on the improvement of polymerase chain reaction. *Nanoscale* **3**, 1741–1747 (2011).
213. Yuce, M. & Budak, H. Dispersion quality of amine functionalized multiwall carbon nanotubes plays critical roles in polymerase chain reaction enhancement. *J. Nanopart. Res.* **16**, 1–13 (2014).
214. Yüce, M., Uysal, E. & Budak, H. Amplification yield enhancement of short DNA templates using bulk and surface-attached amine-functionalized single-wall carbon nanotubes. *Appl. Surf. Sci.* **349**, 147–155 (2015).
215. Khaliq, A., Kafafy, R., Salleh, H. M. & Faris, W. F. Enhancing the efficiency of polymerase chain reaction using graphene nanoflakes. *Nanotechnology* **23**, 455106 (2012).
216. Khaliq, A. et al. Enhancement in the efficiency of polymerase chain reaction by TiO_2 nanoparticles: crucial role of enhanced thermal conductivity. *Nanotechnology* **21**, 255704 (2010).
217. Fadhil, A., Al-Jeboory, M. & Al-Jailawi, M. Improving and enhancement of PCR amplification by using ZnO and TiO_2 nanoparticles. *Int. J. Curr. Microbiol. Appl. Sci.* **3**, 549–557 (2014).
218. Dantas, P. V. P., Melo, C. F., Houllou, L. M. & Machado, G. Nanoparticle-assisted Polymerase Chain Reaction (NanoPCR): Optimization of PCR detection of Leifsonia xyli subsp. xyli by the addition of nanoparticles. *J. Appl. Adv. Res.* **2**, 13–20 (2017).
219. Ma, W. et al. A PCR based magnetic assembled sensor for ultrasensitive DNA detection. *Chem. Commun.* **49**, 5369–5371 (2013).

220. Kambli, P. & Kelkar-Mane, V. Nanosized Fe_3O_4 an efficient PCR yield enhancer—comparative study with Au, Ag nanoparticles. *Colloids Surf. B: Biointerfaces* **141**, 546–552 (2016).
221. Park, J. Y. et al. Dopamine-assisted synthesis of carbon-coated silica for PCR enhancement. *ACS Appl. Mater. Interfaces* **7**, 15633–15640 (2015).
222. Fuming, S., Yang, Y., Hexiang, Z., Meirong, M. & Zhizhou, Z. CdTe quantum dots accelerate the speed of Pfu-based polymerase chain reaction. *J. Exp. Nanosci.* **10**, 476–482 (2015).
223. Sang, F., Zhang, Z., Yuan, L. & Liu, D. Quantum dots for a high-throughput Pfu polymerase based multi-round polymerase chain reaction (PCR). *Analyst* **143**, 1259–1267 (2018).
224. Zhu, M. et al. Interactions of the primers and Mg 2+ with graphene quantum dots enhance PCR performance. *RSC Adv.* **5**, 74515–74522 (2015).
225. Xia, J. et al. Polydopamine nanospheres-assisted direct PCR for rapid detection of Escherichia coli O157: H7. *Anal. Biochem.* **654**, 114797 (2022).
226. Kim, H. R., Baek, A., Lee, I. J. & Kim, D.-E. Facilitation of polymerase chain reaction with poly (ethylene glycol)-engrafted graphene oxide analogous to a single-stranded-DNA binding protein. *ACS Appl. Mater. interfaces* **8**, 33521–33528 (2016).
227. Sun, C. et al. Efficient polymerase chain reaction assisted by metal–organic frameworks. *Chem. Sci.* **11**, 797–802 (2020).
228. Cui, Y., Wang, Z., Ma, X., Liu, J. & Cui, S. A sensitive and specific nanoparticle-assisted PCR assay for rapid detection of porcine parvovirus. *Lett. Appl. Microbiol.* **58**, 163–167 (2014).
229. Ma, X., Cui, Y., Qiu, Z., Zhang, B. & Cui, S. A nanoparticle-assisted PCR assay to improve the sensitivity for rapid detection and differentiation of wild-type pseudorabies virus and gene-deleted vaccine strains. *J. Virological Methods* **193**, 374–378 (2013).
230. Wang, X. et al. A new nanoPCR molecular assay for detection of porcine bocavirus. *J. Virological Methods* **202**, 106–111 (2014).
231. Yuan, W. et al. Development of a nanoparticle-assisted PCR assay for detection of porcine epidemic diarrhea virus. *J. Virological Methods* **220**, 18–20 (2015).
232. Wang, J. et al. Development of a nanoparticle-assisted PCR (nanoPCR) assay for detection of mink enteritis virus (MEV) and genetic characterization of the NS1 gene in four Chinese MEV strains. *BMC Vet. Res.* **11**, 1–8 (2015).
233. Luo, Y., Liang, L., Zhou, L., Zhao, K. & Cui, S. Concurrent infections of pseudorabies virus and porcine bocavirus in China detected by duplex nanoPCR. *J. Virological Methods* **219**, 46–50 (2015).
234. El-Husseini, D., Helmy, N. & Tammam, R. The effect of gold nanoparticles on the diagnostic polymerase chain reaction technique for equine herpes virus 1 (EHV-1). *RSC Adv.* **6**, 54898–54903 (2016).
235. Yuan, W., Li, Y., Wang, J., Wang, J. & Sun, J. A nanoparticle-assisted PCR assay for the detection of encephalomyocarditis virus. *Veterinarski Arh.* **86**, 1–8 (2016).
236. Zhu, Y. et al. A sensitive duplex nanoparticle-assisted PCR assay for identifying porcine epidemic diarrhea virus and porcine transmissible gastroenteritis virus from clinical specimens. *Virus Genes* **53**, 71–76 (2017).
237. Liu, Z. et al. Development of a nanoparticle-assisted PCR assay for detection of bovine respiratory syncytial virus. *BMC Vet. Res.* **15**, 1–6 (2019).
238. Wang, M. et al. Simultaneous detection of bovine rotavirus, bovine parvovirus, and bovine viral diarrhea virus using a gold nanoparticle-assisted PCR assay with a dual-priming oligonucleotide system. *Front. Microbiol.* **10**, 2884 (2019).
239. Ma, X., Li, Y., Liu, R., Wei, W. & Ding, C. Development of a sensitive and specific nanoparticle- assisted PCR assay for detecting HPV-16 and HPV-18 DNA. *J. Med. Virol.* **92**, 3793–3798 (2020).
240. Qin, T., Wang, J. & Cui, S.-J. Development of a nanoparticle-assisted PCR assay to distinguish canine coronaviruses I and II. *J. Vet. Diagnostic Investig.* **33**, 104–107 (2021).
241. Wang, Y. et al. A multiplex nanoparticle-assisted polymerase chain reaction assay for detecting three canine epidemic viruses using a dual priming oligonucleotide system. *J. Virological Methods* **298**, 114290 (2021).
242. Ma, H. et al. Development and evaluation of NanoPCR for the detection of Goose Parvovirus. *Vet. Sci.* **9**, 460 (2022).
243. Xue, H. et al. Development and application of nanoPCR method for detection of Feline Panleukopenia Virus. *Vet. Sci.* **10**, 440 (2023).
244. Jeong, S. et al. Extraction of viral nucleic acids with carbon nanotubes increases SARS-CoV-2 quantitative reverse transcription polymerase chain reaction detection sensitivity. *ACS Nano* **15**, 10309–10317 (2021).
245. Devika, P. et al. Nano-PCR for the early detection of tomato leaf curl virus. *3 Biotech* **14**, 5 (2024).
246. Kim, J.-W., Kim, M., Lee, K. K., Chung, K. H. & Lee, C.-S. Effects of graphene oxide- gold nanoparticles nanocomposite on highly sensitive foot-and-mouth disease virus detection. *Nanomaterials* **10**, 1921 (2020).
247. Chia-Ching, L., Subramaniam, S., Sivasubramanian, S. & Feng-Huei, L. MWCNT-Fe_3O_4- based immuno-PCR for the early screening of nasopharyngeal carcinoma. *Mater. Sci. Eng. C* **61**, 422–428 (2016).
248. Upadhyay, A. et al. ZnO nanoflower-based NanoPCR as an efficient diagnostic tool for quick diagnosis of canine vector-borne pathogens. *Pathogens* **9**, 122 (2020).
249. Kim, S.-K. et al. Nanoparticle-based visual detection of amplified DNA for diagnosis of hepatitis c virus. *Biosensors* **12**, 744 (2022).
250. Xu, S. & Yao, M. NanoPCR detection of bacterial aerosols. *J. Aerosol Sci.* **65**, 1–9 (2013).
251. Gabriel, S. et al. Development of nanoparticle-assisted PCR assay in the rapid detection of brain-eating amoebae. *Parasitol. Res.* **117**, 1801–1811 (2018).
252. Xue, Z. et al. Taqman-MGB nanoPCR for highly specific detection of single-base mutations. *Int. J. Nanomed.* **16**, 3695–3705 (2021).
253. Roche, P. J. et al. Demonstration of a plasmonic thermocycler for the amplification of human androgen receptor DNA. *Analyst* **137**, 4475–4481 (2012).
254. Lee, J.-H. et al. Plasmonic photothermal gold bipyramid nanoreactors for ultrafast real-time bioassays. *J. Am. Chem. Soc.* **139**, 8054–8057 (2017).
255. Jiang, K. et al. Plasmonic colorimetric PCR for Rapid molecular diagnostic assays. *Sens. Actuators B: Chem.* **337**, 129762 (2021).
256. Blumenfeld, N. R. et al. Multiplexed reverse-transcriptase quantitative polymerase chain reaction using plasmonic nanoparticles for point-of-care COVID-19 diagnosis. *Nat. Nanotechnol.* **17**, 984–992 (2022).
257. Ahn, J. S., Park, W., Jeong, D. H., Choi, S. B. & Ahn, S. H. Rapid quantitative PCR equipment using photothermal conversion of Au nanoshell. *Sci. Rep.* **14**, 3895 (2024).
258. Li, T.-J. et al. Handheld energy-efficient magneto-optical real-time quantitative PCR device for target DNA enrichment and quantification. NPG Asia. *Materials* **8**, e277–e277 (2016).
259. Kim, B. K. et al. Ultrafast real-time pcr in photothermal microparticles. *ACS Nano* **16**, 20533–20544 (2022).
260. Shrestha, K. et al. Mobile efficient diagnostics of infectious diseases via On-Chip RT-qPCR: MEDIC-PCR. Advanced. *Adv. Sci.* **10**, 2302072 (2023).
261. Arami, H. et al. Remotely controlled near-infrared-triggered photothermal treatment of brain tumours in freely behaving mice using gold nanostar s. *Nat. Nanotechnol.* **17**, 1015–1022 (2022).
262. Chen, C. et al. A Janus Au–polymersome heterostructure with near-field enhancement effect for implant-associated infection phototherapy. *Adv. Mater.* **35**, 2207950 (2023).
263. He, J. et al. SERS/NIR-II optical nanoprobes for multidimensional tumor imaging from living subjects, pathology, and single cells and guided NIR-II photothermal therapy. *Adv. Funct. Mater.* **32**, 2208028 (2022).
264. Chen, X. et al. Triangular pyramid nanostructure enhanced photothermal utilization of noble metal nanoparticles. *Int. J. Therm. Sci.* **200**, 108980 (2024).
265. Li, S. et al. Tensile-strained palladium nanosheets for synthetic catalytic therapy and phototherapy. *Adv. Mater.* **34**, 2202609 (2022).
266. De Marchi, S., Núñez-Sánchez, S., Bodelón, G., Pérez-Juste, J. & Pastoriza-Santos, I. Pd nanoparticles as a plasmonic material: synthesis, optical properties and applications. *Nanoscale* **12**, 23424–23443 (2020).
267. You, Q. et al. Pd8 nanocluster with nonmetal-to-metal-ring coordination and promising photothermal conversion efficiency. *Angew. Chem.* **136**, e202313491 (2024).
268. Xiao, J.-W. et al. Porous Pd nanoparticles with high photothermal conversion efficiency for efficient ablation of cancer cells. *Nanoscale* **6**, 4345–4351 (2014).
269. Feng, E. et al. Fine-tuning Cu (II)-induced self-assembly of hydrophilic cyanine dyes for enhanced tumor photothermal therapy. *Adv. Funct. Mater.* **32**, 2209258 (2022).
270. Chang, M. et al. Cu single atom nanozyme based high-efficiency mild photothermal therapy through cellular metabolic regulation. *Angew. Chem.* **134**, e202209245 (2022).
271. Chen, S., Tang, F., Tang, L. & Li, L. Synthesis of Cu-nanoparticle hydrogel with self-healing and photothermal properties. *ACS Appl. Mater. Interfaces* **9**, 20895–20903 (2017).
272. Li, K.-C., Chu, H.-C., Lin, Y., Tuan, H.-Y. & Hu, Y.-C. PEGylated copper nanowires as a novel photothermal therapy agent. *ACS Appl. Mater. Interfaces* **8**, 12082–12090 (2016).

273. Wang, J. et al. Synthesis of copper nanoparticles with controllable crystallinity and their photothermal property. *Colloids Surf. A: Physicochem. Eng. Asp.* **626**, 126970 (2021).
274. Ye, J. et al. Tumor response and NIR-II photonic thermal co-enhanced catalytic therapy based on single-atom manganese nanozyme. *Adv. Funct. Mater.* **32**, 2206157 (2022).
275. Li, J. et al. Manganese coordination micelles that activate stimulator of interferon genes and capture in situ tumor antigens for cancer metalloimmunotherapy. *ACS Nano* **16**, 16909–16923 (2022).
276. Xu, Y. et al. Sheet-like 2D manganese (IV) complex with high photothermal conversion efficiency. *J. Am. Chem. Soc.* **144**, 18834–18843 (2022).
277. Li, Z. et al. Mangasese doped polypyrole nanoparticels for photothermal/chemodynamic therapy and immune activation. *Nanotechnology* **34**, 055102 (2022).
278. Fluksman, A. et al. Efficient tumor eradication at ultralow drug concentration via externally controlled and boosted metallic iron magnetoplasmonic nanocapsules. *ACS Nano* **17**, 1946–1958 (2022).
279. Liu, H. et al. Fe (iii)-doped polyaminopyrrole nanoparticle for imaging-guided photothermal therapy of bladder cancer. *ACS Biomater. Sci. Eng.* **8**, 502–511 (2022).
280. Xu, N. et al. Fe (III)-chelated polydopamine nanoparticles for synergistic tumor therapies of enhanced photothermal ablation and antitumor immune activation. *ACS Appl. Mater. Interfaces* **14**, 15894–15910 (2022).
281. Yu, H. et al. A self-assembled metal-polyphenolic nanomedicine for mild photothermal-potentiated chemodynamic therapy of tumors. *Appl. Mater. Today* **25**, 101235 (2021).
282. Liu, Y. et al. One-dimensional Fe_2P acts as a Fenton agent in response to NIR II light and ultrasound for deep tumor synergetic theranostics. *Angew. Chem.* **131**, 2429–2434 (2019).
283. Ye, Y. et al. Cell wall destruction and internal cascade synergistic antifungal strategy for fungal keratitis. *ACS Nano* **16**, 18729–18745 (2022).
284. Chen, J. et al. Space-confined seeded growth of black silver nanostructures for solar steam generation. *Nano Lett.* **19**, 400–407 (2018).
285. Nie, C. et al. Ag@ TiO_2 nanoprisms with highly efficient near-infrared photothermal conversion for melanoma therapy. *Chem.— Asian J.* **15**, 148–155 (2020).
286. Bian, K. et al. Peptide-directed hierarchical mineralized silver nanocages for anti-tumor photothermal therapy. *ACS Sustain. Chem. Eng.* **6**, 7574–7588 (2018).
287. Qi, X. et al. Engineering robust Ag-decorated polydopamine nano-photothermal platforms to combat bacterial infection and prompt wound healing. *Adv. Sci.* **9**, 2106015 (2022).
288. Sun, L. et al. Phase-transition induced conversion into a photothermal material: quasi- metallic $WO_{2.\ 9}$ nanorods for solar water evaporation and anticancer photothermal therapy. *Angew. Chem. Int. Ed.* **57**, 10666–10671 (2018).
289. Chen, K. et al. Tunable NIR absorption property of a dithiolene nickel complex: a promising NIR-II absorption material for photothermal therapy. *ACS Appl. Bio Mater.* **4**, 4406–4412 (2021).
290. Feng, Y. et al. Mace-like plasmonic au-pd heterostructures boost near-infrared photoimmunotherapy. *Adv. Science* **10**, 2204842 (2023).
291. Li, K. et al. Ultrathin nanosheet-supported Ag@ Ag_2O core–shell nanoparticles with vastly enhanced photothermal conversion efficiency for NIR-II-triggered photothermal therapy. *ACS Biomater. Sci. Eng.* **8**, 540–550 (2022).
292. Hu, Y. et al. Multifunctional Fe_3O_4@ Au core/shell nanostars: a unique platform for multimode imaging and photothermal therapy of tumors. *Sci. Rep.* **6**, 28325 (2016).
293. Zhang, Y. et al. Pd@ Au bimetallic nanoplates decorated mesoporous MnO_2 for synergistic nucleus-targeted NIR-II photothermal and hypoxia-relieved photodynamic therapy. Advanced Healthcare. *Adv. Healthcare Mater.* **9**, 1901528 (2020).
294. Tang, J. et al. Au@ Pt nanostructures: a novel photothermal conversion agent for cancer therapy. *Nanoscale* **6**, 3670–3678 (2014).
295. Leng, C. et al. Engineering gold nanorod–copper sulfide heterostructures with enhanced photothermal conversion efficiency and photostability. *Small* **14**, 1703077 (2018).
296. Ayala-Orozco, C. et al. Au nanomatryoshkas as efficient near-infrared photothermal transducers for cancer treatment: benchmarking against nanoshells. *ACS Nano* **8**, 6372–6381 (2014).
297. Xu, C. et al. Bacteria-like mesoporous silica-coated gold nanorods for positron emission tomography and photoacoustic imaging-guided chemo-photothermal combined therapy. *Biomaterials* **165**, 56–65 (2018).
298. Liu, S. et al. Biomimetic nanobomb for synergistic therapy with inhibition of cancer stem cells. *Small* **19**, 2206503 (2023).
299. Li, H. et al. Photothermal-triggered release of alkyl radicals and cascade generation of hydroxyl radicals via a versatile hybrid nanocatalyst for hypoxia-irrelevant synergistic antibiofilm therapy. *Chem. Eng. J.* **455**, 140903 (2023).
300. Liu, J., Feng, L. & Wu, Y. Enzymatically synthesised MnO_2 nanoparticles for efficient near-infrared photothermal therapy and dual-responsive magnetic resonance imaging. *Nanoscale* **13**, 11093–11103 (2021).
301. Zeng, D. et al. Synergistic photothermal/photodynamic suppression of prostatic carcinoma by targeted biodegradable MnO_2 nanosheets. *Drug Deliv.* **26**, 661–672 (2019).
302. Wang, L. et al. Highly efficient vacancy-driven photothermal therapy mediated by ultrathin MnO_2 nanosheets. *ACS Appl. Mater. interfaces* **11**, 6267–6275 (2019).
303. Shaw, S. et al. γ-Fe_2O_3 nanoflowers as efficient magnetic hyperthermia and photothermal agent. *Appl. Surf. Sci.* **560**, 150025 (2021).
304. Yang, B. et al. Modulated ultrasmall γ-Fe_2O_3 nanocrystal assemblies for switchable magnetic resonance imaging and photothermal-ferroptotic-chemical synergistic cancer therapy. *Adv. Funct. Mater.* **33**, 2211251 (2023).
305. Qin, W. et al. Protease-Activatable nanozyme with photoacoustic and tumor-enhanced magnetic resonance imaging for photothermal ferroptosis cancer therapy. *Adv. Funct. Mater.* **33**, 2209748 (2023).
306. Zhu, W. et al. Photothermal nanozyme-based microneedle patch against refractory bacterial biofilm infection via iron-actuated Janus ion therapy. *Adv. Mater.* **34**, 2207961 (2022).
307. Guan, G. et al. High-efficiency and safe sulfur-doped iron oxides for magnetic resonance imaging-guided photothermal/magnetic hyperthermia therapy. *Dalton Trans.* **49**, 5493–5502 (2020).
308. Zhang, P. et al. Nanoprobe based on biominerals in protein corona for dual-modality MR imaging and therapy of tumors. *ACS Nano* **17**, 184–196 (2022).
309. Xiong, K. et al. Ag_2S decorated nanocubes with enhanced near-infrared photothermal and photodynamic properties for rapid sterilization. *Colloid Interface Sci. Commun.* **33**, 100201 (2019).
310. Zhao, J., Zhang, Q., Liu, W., Shan, G. & Wang, X. Biocompatible BSA-Ag_2S nanoparticles for photothermal therapy of cancer. *Colloids Surf. B: Biointerfaces* **211**, 112295 (2022).
311. Han, R. et al. Ag_2S nanoparticles as an emerging single-component theranostic agent. *Chin. Chem. Lett.* **31**, 1717–1728 (2020).
312. Munaro, J. et al. The role of the synthetic pathways on properties of Ag_2S nanoparticles for photothermal applications. *Appl. Surf. Sci.* **514**, 145856 (2020).
313. Zhao, H. et al. NIR-II light leveraged dual drug synthesis for orthotopic combination therapy. *ACS Nano* **16**, 20353–20363 (2022).
314. Li, B. et al. $Cu_{7.2}S_4$ nanocrystals: a novel photothermal agent with a 56.7% photothermal conversion efficiency for photothermal therapy of cancer cells. *Nanoscale* **6**, 3274–3282 (2014).
315. Liu, X. et al. Facile synthesis of biocompatible cysteine-coated CuS nanoparticles with high photothermal conversion efficiency for cancer therapy. *Dalton Trans.* **43**, 11709–11715 (2014).
316. Qiu, S. et al. A smart nanoreactor based on an O_2-economized dual energy inhibition strategy armed with dual multi-stimuli-responsive "Doorkeepers" for Enhanced CDT/PTT of rheumatoid arthritis. *ACS Nano* **16**, 17062–17079 (2022).
317. Yong, Y. et al. WS_2 nanosheet as a new photosensitizer carrier for combined photodynamic and photothermal therapy of cancer cells. *Nanoscale* **6**, 10394–10403 (2014).
318. Geng, B. et al. Carbon dot/WS_2 heterojunctions for NIR-II enhanced photothermal therapy of osteosarcoma and bone regeneration. *Chem. Eng. J.* **383**, 123102 (2020).
319. Cui, X.-Z. et al. PEGylated WS_2 nanosheets for X-ray computed tomography imaging and photothermal therapy. *Chin. Chem. Lett.* **26**, 749–754 (2015).
320. Yan, H. et al. Ultrathin porous nitrogen-doped carbon-coated CuSe Heterostructures for com- bination Cancer therapy of Photothermal therapy, photocatalytic therapy, and logic-gated chemotherapy. *ACS Appl. Mater. Interfaces* **14**, 56237–56252 (2022).
321. Hu, C., Zhang, Z., Liu, S., Liu, X. & Pang, M. Monodispersed CuSe sensitized covalent organic framework photosensitizer with an enhanced photodynamic and photothermal effect for cancer therapy. *ACS Appl. Mater. interfaces* **11**, 23072–23082 (2019).

322. Wang, X. et al. One-pot solution synthesis of shape-controlled copper selenide nanostructures and their potential applications in photocatalysis and photothermal therapy. *Nanoscale* **9**, 14512–14519 (2017).
323. Xie, H. et al. Metabolizable ultrathin Bi_2Se_3 nanosheets in imaging-guided photothermal therapy. *Small* **12**, 4136–4145 (2016).
324. Wang, Y. et al. BSA-mediated synthesis of bismuth sulfide nanotheranostic agents for tumor multimodal imaging and thermoradiotherapy. *Adv. Funct. Mater.* **26**, 5335–5344 (2016).
325. Zhang, C. et al. Rod-based urchin-like hollow microspheres of Bi_2S_3: facile synthesis, photocontrolled drug release for photoacoustic imaging and chemo-photothermal therapy of tumor ablation. *Biomaterials* **237**, 119835 (2020).
326. Wang, J. et al. Biodegradable ferrous sulfide-based nanocomposites for tumor theranostics through specific intratumoral acidosis-induced metabolic symbiosis disruption. *J. Am. Chem. Soc.* **144**, 19884–19895 (2022).
327. Meng, Z. et al. Design and synthesis of "all-in-one" multifunctional FeS_2 nanoparticles for magnetic resonance and near-infrared imaging guided photothermal therapy of tumors. *Adv. Funct. Mater.* **26**, 8231–8242 (2016).
328. Xiao, S. et al. Multifunctional FeS_2 theranostic nanoparticles for photothermal-enhanced chemodynamic/photodynamic cancer therapy and photoacoustic imaging. *Chem. Eng. J.* **396**, 125294 (2020).
329. Wang, D. et al. Helical bowl-like SnS_2 with structure-induced conversion efficiency for enhanced photothermal therapy. *Chem. Eng. J.* **400**, 125814 (2020).
330. Yang, J. et al. Ag functionalized SnS_2 with enhanced photothermal activity for safe and efficient wound disinfection. Biomaterials. *Science* **9**, 4728–4736 (2021).
331. Zhen, W. et al. BSA-IrO_2: catalase-like nanoparticles with high photothermal conversion efficiency and a high X-ray absorption coefficient for anti-inflammation and antitumor theranostics. *Angew. Chem.* **130**, 10466–10470 (2018).
332. Xiong, Y. et al. A biomimetic one-pot synthesis of versatile Bi_2S_3/FeS_2 theranostic nanohybrids for tumor-targeted photothermal therapy guided by CT/MR dual-modal imaging. *Chem. Eng. J.* **378**, 122172 (2019).
333. Jiang, Q. et al. Broadband absorption and enhanced photothermal conversion property of octopod-like Ag@ Ag_2S core@ shell structures with gradually varying shell thickness. *Sci. Rep.* **7**, 17782 (2017).
334. Wang, M. et al. Rational design of multifunctional Fe@ γ-Fe_2O_3@ H-TiO_2 nanocomposites with enhanced magnetic and photoconversion effects for wide applications: from photocatalysis to imaging-guided photothermal cancer therapy. *Adv. Mater.* **30**, 1706747 (2018).
335. Luo, B. et al. Systematic investigating on the broadband solar absorption and photo-thermal conversion performance of TiN@ rGO plasmonic nanofluids. *Colloids Surf. A: Physicoch. Eng. Asp.* **630**, 127549 (2021).
336. Wang, X. et al. Amino acid-mediated amorphous copper sulphide with enhanced photothermal conversion efficiency for antibacterial application. *J. Colloid Interface Sci.* **657**, 142–154 (2024).
337. Pan, J. et al. Fluorescent phthalocyanine–graphene conjugate with enhanced NIR absorbance for imaging and multi-modality therapy. *ACS Appl. Nano Mater.* **1**, 2785–2795 (2018).
338. Wang, Y. et al. Three dimensional mesoporous carbon nanospheres as carriers for chemo-photothermal therapy compared with two dimensional graphene oxide nanosheets. *Colloids Surf. A: Physicochem. Eng. Asp.* **590**, 124498 (2020).
339. Li, X. et al. Graphene oxide-based efficient and scalable solar desalination under one sun with a confined 2D water path. *Proc. Natl Acad. Sci.* **113**, 13953–13958 (2016).
340. Hu, X. et al. Tailoring graphene oxide-based aerogels for efficient solar steam generation under one sun. *Adv. Mater. (Deerfield Beach, FL)* **29** (2016).
341. Liu, S., Huang, C., Luo, X. & Rao, Z. High-performance solar steam generation of a paper-based carbon particle system. *Appl. Therm. Eng.* **142**, 566–572 (2018).
342. Wang, X. et al. The multifunctional Prussian blue/graphitic carbon nitride nanocomposites for fluorescence imaging-guided photothermal and photodynamic combination therapy. *RSC Adv.* **13**, 335–343 (2023).
343. Zhao, Y. et al. Temperature-sensitive lipid-coated carbon nanotubes for synergistic photothermal therapy and gene therapy. *ACS Nano* **15**, 6517–6529 (2021).
344. Bao, Y., Huang, A., Zheng, X. & Qin, G. Enhanced photothermal conversion performance of MWCNT/SiC hybrid aqueous nanofluids in direct absorption solar collectors. *J. Mol. Liq.* **387**, 122577 (2023).
345. Wang, Y., Wang, C., Song, X., Megarajan, S. K. & Jiang, H. A facile nanocomposite strategy to fabricate a rGO–MWCNT photothermal layer for efficient water evaporation. *J. Mater. Chem. A* **6**, 963–971 (2018).
346. Permatasari, F. A., Fukazawa, H., Ogi, T., Iskandar, F. & Okuyama, K. Design of pyrrolic-N- rich carbon dots with absorption in the first near-infrared window for photothermal therapy. *ACS Appl. Nano Mater.* **1**, 2368–2375 (2018).
347. Zhu, X. et al. Temperature-feedback upconversion nanocomposite for accurate photothermal therapy at facile temperature. *Nat. Commun.* **7**, 1–10 (2016).
348. Moniruzzaman, M., Dutta, S. D., Lim, K-T. & Kim, J. Perylene-derived hydrophilic carbon dots with polychromatic emissions as superior bioimaging and NIR-responsive photothermal bactericidal agent. *ACS Omega* **7**, 37388–37400 (2022).
349. Zheng, M. et al. One-pot to synthesize multifunctional carbon dots for near infrared fluorescence imaging and photothermal cancer therapy. *ACS Appl. Mater. interfaces* **8**, 23533–23541 (2016).
350. Geng, B. et al. NIR-responsive carbon dots for efficient photothermal cancer therapy at low power densities. *Carbon* **134**, 153–162 (2018).
351. Peng, X. et al. Carbon dots/Prussian blue satellite/core nanocomposites for optical imaging and photothermal therapy. *ACS Appl. Mater. interfaces* **10**, 1084–1092 (2018).
352. Wei, C., Jin, X., Wu, C., Brozovic, A. & Zhang, W. Carbon spheres with high photothermal conversion efficiency for photothermal therapy of tumor. *Diam. Relat. Mater.* **126**, 109048 (2022).
353. Xue, G. et al. Robust and low-cost flame-treated wood for high-performance solar steam generation. *ACS Appl. Mater. interfaces* **9**, 15052–15057 (2017).
354. Xu, N. et al. Mushrooms as efficient solar steam-generation devices. *Adv. Mater.* **29**, 1606762 (2017).
355. Xie, M. et al. Construction of an integrated multi-layer textile for solar-driven steam generation. *Appl. Opt.* **60**, 4930–4937 (2021).
356. Wu, J. et al. Enzyme-engineered conjugated polymer nanoplatform for activatable companion diagnostics and multistage augmented synergistic therapy. *Adv. Mater.* **34**, 2200062 (2022).
357. Duan, X. et al. Semiconducting polymer nanoparticles with intramolecular motion-induced photothermy for tumor phototheranostics and tooth root canal therapy. *Adv. Mater.* **34**, 2200179 (2022).
358. Qian, W. et al. pH-triggered charge-reversible of glycol chitosan conjugated carboxyl graphene for enhancing photothermal ablation of focal infection. *Acta Biomater.* **69**, 256–264 (2018).
359. Xu, W. et al. Flexible and salt resistant Janus absorbers by electrospinning for stable and efficient solar desalination. *Adv. Energy Mater.* **8**, 1702884 (2018).
360. Chang, R. et al. Amino-acid-encoded supramolecular photothermal nanomedicine for enhanced cancer therapy. *Adv. Mater.* **34**, 2200139 (2022).
361. Guo, X. et al. Unique double intramolecular and intermolecular exciton coupling in ethene-bridged aza-BODIPY dimers for high-efficiency near-infrared photothermal conversion and therapy. *Angew. Chem. Int. Ed.* **61**, e202211081 (2022).
362. Li, Y. et al. Incorporation of robust NIR-II fluorescence brightness and photothermal performance in a single large π-conjugated molecule for phototheranostics. *SAdv. Sci.* **10**, 2204695 (2023).
363. Bian, H. et al. Cardiolipin-targeted NIR-II fluorophore causes "Avalanche effects" for re- engaging cancer apoptosis and inhibiting metastasis. *J. Am. Chem. Soc.* **144**, 22562–22573 (2022).
364. Chen, S. et al. Increasing molecular planarity through donor/side-chain engineering for improved NIR-IIa fluorescence imaging and NIR-II photothermal therapy under 1064 nm. *Angew. Chem.* **135**, e202215372 (2023).
365. Xu, G. et al. A supramolecular photosensitizer derived from an Arene-Ru (II) complex self-assembly for NIR activated photodynamic and photothermal therapy. *Nat. Commun.* **13**, 3064 (2022).
366. Li, C. et al. Fluorination enhances NIR-II emission and photothermal conversion efficiency of phototheranostic agents for imaging-guided cancer therapy. *Adv. Mater.* **35**, 2208229 (2023).
367. Wang, J. et al. A smart photothermal nanosystem with an intrinsic temperature-control mechanism for thermostatic treatment of bacterial infections. *Adv. Mater.* **34**, 2205653 (2022).
368. Wen, K. et al. Achieving efficient NIR-II type-I photosensitizers for photodynamic/photothermal therapy upon regulating chalcogen elements. *Adv. Mater.* **34**, 2108146 (2022).
369. Chen, P. et al. Bandgap modulation and lipid intercalation generates ultrabright D–A–D-based zwitterionic small-molecule nanoagent for precise

NIR-II excitation phototheranostic applications. *Adv. Funct. Mater.* **32**, 2208463 (2022).
370. Liu, J. et al. Molecular oligomerization and donor engineering strategies for achieving superior NIR-II fluorescence imaging and thermotherapy under 1064 nm laser irradiation. *Small* **19**, 2205640 (2023).
371. Xiao, P. et al. De novo design of reversibly PH-switchable NIR-II aggregation-induced emission luminogens for efficient phototheranostics of patient-derived tumor xenografts. *J. Am. Chem. Soc.* **145**, 334–344 (2022).
372. Bai, Y. et al. Treat the "Untreatable" by a photothermal agent: triggering heat and immuno-logical responses for rabies virus inactivation. *Adv. Science* **10**, 2205461 (2023).
373. Ma, X. et al. J-aggregates formed by NaCl treatment of aza-coating heptamethine cyanines and their application to monitoring salt stress of plants and promoting photothermal therapy of tumors. *Angew. Chem. Int. Ed.* **62**, e202216109 (2023).
374. Liu, K., Jiang, Z., Lalancette, R. A., Tang, X. & Jäkle, F. Near-infrared-absorbing B–N lewis pair-functionalized anthracenes: electronic structure tuning, conformational isomerism, and applications in photothermal cancer therapy. *J. Am. Chem. Soc.* **144**, 18908–18917 (2022).
375. Chen, Y. et al. Glutathione-depleting organic metal adjuvants for effective NIR-II photothermal immunotherapy. *Adv. Mater.* **34**, 2201706 (2022).